Merger of black hole and neutron star in general relativity: Tidal disruption, torus mass, and gravitational waves

Masaru Shibata

Graduate School of Arts and Sciences, University of Tokyo, Komaba, Meguro, Tokyo 153-8902, Japan

Keisuke Taniguchi

Department of Physics, University of Illinois at Urbana-Champaign, Urbana, Illinois 61801, USA

(Received 31 October 2007; published 17 April 2008)

We study the properties of the merger of black hole–neutron star (BH-NS) binaries in fully general relativistic simulation, focusing on the case that the NS is tidally disrupted. We prepare BH-NS binaries in a quasicircular orbit as the initial condition in which the BH is modeled by a nonspinning moving puncture. For modeling the NS, we adopt the Γ-law equation of state with $\Gamma = 2$ and the irrotational velocity field. We change the BH mass in the range $M_{\rm BH} \approx 3.3M_\odot$–$4.6M_\odot$, while the rest mass of the NS is fixed to be $M_* = 1.4M_\odot$ (i.e., the NS mass $M_{\rm NS} \approx 1.3M_\odot$). The radius of the corresponding spherical NS is set in the range $R_{\rm NS} \approx 12$–15 km (i.e., the compactness $GM_{\rm NS}/R_{\rm NS}c^2 \approx 0.13$–$0.16$). We find for all the chosen initial conditions that the NS is tidally disrupted near the innermost stable circular orbit. The numerical results indicate that, for the model of $R_{\rm NS} = 12$ km, more than $\sim 95\%$ of the rest mass is quickly swallowed by the BH and the resultant torus mass surrounding the BH is less than $\sim 0.05M_\odot$. For the model of $R_{\rm NS} \approx 14.7$ km, by contrast, the torus mass is $\sim 0.15M_\odot$ for the BH mass $\approx 4M_\odot$. The thermal energy of the material in the torus increases due to the shock heating that occurs in the collision between the spiral arms, resulting in the temperature 10^{10}–10^{11} K. Our results indicate that the merger between a low-mass BH and its companion NS may form a central engine of short gamma-ray bursts of the total energy of order 10^{49} ergs if the compactness of the NS is fairly small, $\lesssim 0.145$. However, for the canonical values $M_{\rm NS} = 1.35M_\odot$ and $R_{\rm NS} = 12$ km, the merger results in small torus mass, and hence it can be a candidate only for the low-energy, short gamma-ray bursts of total energy of order 10^{48} ergs. We also present gravitational waveforms during the inspiral, tidal disruption of the NS, and subsequent evolution of the disrupted material. We find that the amplitude of gravitational waves quickly decreases after the onset of tidal disruption. Although the quasinormal mode is excited, its gravitational wave amplitude is much smaller than that of the late inspiral phase. This is reflected in the fact that the spectrum amplitude sharply falls above a cutoff frequency which is determined by the tidal disruption process. We also find that the cutoff frequency is 1.25–1.4 times larger than the frequency predicted by the study for the sequence of the quasicircular orbits, and this factor of the deviation depends on the compactness of the NS.

DOI: 10.1103/PhysRevD.77.084015 PACS numbers: 04.25.dg, 04.25.dk, 04.30.−w, 04.40.Dg

I. INTRODUCTION

The merger of black hole (BH)–neutron star (NS) binaries is one of the most promising sources of kilometer-size laser interferometric gravitational wave detectors such as LIGO and VIRGO. Although such a system has not been observed yet in our Galaxy, in contrast to NS-NS binaries [1], statistical studies based on the stellar evolution synthesis suggest that the merger will happen 1%–10% as frequently as the merger of the NS-NS binaries in the universe [2]. Because the BH mass should be more than twice as large as the canonical NS mass $\sim 1.35M_\odot$, the typical amplitude of gravitational waves from the BH-NS binaries will be larger than that from the NS-NS binaries even if the distance is larger. This indicates that the detection rate of the BH-NS binaries by the gravitational wave detectors may be more than 10% as high as that for the NS-NS binaries, suggesting that the detection of such a system will be achieved in the near future.

The final fate of the BH-NS binaries is divided into two cases depending primarily on the BH mass: (1) when the BH mass is small enough, the NS will be tidally disrupted before it is swallowed by the BH; (2) when the BH mass is large enough, the NS will be swallowed by the BH without tidal disruption. The tidal disruption occurs when the tidal force of the BH is stronger than the self-gravity of the NS. Such condition is approximately written as

$$\frac{M_{\rm BH}R_{\rm NS}}{r^3} \geq C^2\frac{M_{\rm NS}}{R_{\rm NS}^2}, \tag{1}$$

where $M_{\rm NS}$ is the NS mass, $R_{\rm NS}$ is the circumferential radius of the NS, $M_{\rm BH}$ is the BH mass, r is the orbital separation, and C is a nondimensional coefficient. Using the orbital angular velocity Ω, Eq. (1) may be written as

$$\Omega^2\frac{M_{\rm BH}}{M_0} \geq C^2\frac{GM_{\rm NS}}{R_{\rm NS}^3}, \tag{2}$$

where G is the gravitational constant and $M_0 = M_{\rm BH} + M_{\rm NS}$. The latest high-precision numerical study for the quasicircular states of the BH-NS binaries shows that the tidal disruption occurs if the following condition is satis-

fied [3,4]:

$$\Omega \geq C\left(\frac{GM_{\rm NS}}{R_{\rm NS}^3}\right)^{1/2}\left(1+\frac{M_{\rm NS}}{M_{\rm BH}}\right)^{1/2}, \quad (3)$$

where the value of C is ≈ 0.270 for a $\Gamma = 2$ polytropic equation of state (EOS). We note that in [3,4] the NS is assumed to be irrotational and the BH spin is set to zero. According to an approximate general relativistic study [5], the value of C depends weakly on the stiffness of the EOSs for $2 \leq \Gamma \leq 3$, and hence it would be close to 0.27 for the NS which likely has such a stiff EOS.

Substituting the typical values considered in this paper, the tidal disruption is expected to set in at

$$\frac{GM_0\Omega}{c^3} = 0.0708\left(\frac{C}{0.270}\right)\left(\frac{M_{\rm NS}}{1.30M_\odot}\right)^{3/2}\left(\frac{R_{\rm NS}}{13.0\ {\rm km}}\right)^{-3/2} \times \left(\frac{q}{1/3}\right)^{-1}\left(\frac{1+q}{4/3}\right)^{3/2}, \quad (4)$$

where c is the speed of light and q denotes the mass ratio $q \equiv M_{\rm NS}/M_{\rm BH}$. The corresponding frequency of gravitational waves is calculated from $f \equiv \Omega/\pi$ as

$$f_{\rm tidal} = 8.79\times 10^2\ {\rm Hz}\left(\frac{C}{0.270}\right)\left(\frac{M_{\rm NS}}{1.30M_\odot}\right)^{1/2} \times \left(\frac{R_{\rm NS}}{13.0\ {\rm km}}\right)^{-3/2}\left(\frac{1+q}{4/3}\right)^{1/2}. \quad (5)$$

According to the third post-Newtonian (PN) study, the innermost stable circular orbit (ISCO) for $q \approx 1/3$ is located at $GM_0\Omega/c^3 \approx 0.11$ [6]. The tidal effect reduces this value slightly to be $GM_0\Omega/c^3 \sim 0.08$–0.09 [3,4]. Adopting this value, we expect that the tidal disruption of the NSs of mass $1.3M_\odot$ occurs for $q \gtrsim 1/4$ if $R_{\rm NS} = 13$ km, and for $q \gtrsim 1/3$ if $R_{\rm NS} = 11$ km. This indicates that the tidal disruption occurs only for the binaries of low-mass BH and NS at an orbit very close to the ISCO.

The tidal disruption of NSs by a BH has been studied with great interest because of the following reasons: (i) Gravitational waves during the tidal disruption may bring information about the NS radius because the orbital frequency at the onset of tidal disruption depends strongly on the compactness of the NS ($GM_{\rm NS}/R_{\rm NS}c^2$) [3–5]. The NS mass will be determined by the data analysis for observed gravitational waves in the inspiral phase [7]. If the NS radius could be determined from observed gravitational waves emitted during the tidal disruption, the resultant relation between the mass and the radius of the NSs may constrain the EOSs of the high-density nuclear matter [8,9]. (ii) The tidally disrupted NSs may form a disk or torus of mass larger than $0.01M_\odot$ around the BH if the tidal disruption occurs outside the ISCO. Systems consisting of a rotating BH surrounded by a massive, hot torus have been proposed as one of the likely sources for the central engine of gamma-ray bursts with a short duration [10] (hereafter, SGRBs). Hence, the merger of a low-mass BH and its companion NS can be a candidate of the central engine. According to the observational results by the *Swift* and *HETE-2* satellites [11], the total energy of the SGRBs is larger than $\sim 10^{48}$ ergs, and typically 10^{49}–10^{50} ergs. The question is whether or not the mass and thermal energy of the torus are large enough for driving the SGRBs of such huge total energy.

The tidal disruption of NSs by a BH has been investigated in the Newtonian [12] and approximately general relativistic [13,14] simulations. However, the criterion of the tidal disruption and the evolution of the tidally disrupted NS material would depend strongly on general relativistic effects around the BH, and hence a simulation in full general relativity is obviously required. In the previous paper [15], we presented our first numerical results for fully general relativistic simulation performed by our new code, which had been improved from the code used for the NS-NS merger [16,17]: We handle an orbiting BH by employing the moving puncture method, which has recently been developed (e.g., [18,19]). We prepared a quasicircular state composed of a nonspinning moving puncture BH and a corotating NS as the initial condition. We computed the BH-NS quasicircular state by employing our new formalism based on the moving puncture framework. From the merger simulation, we found that a torus with mass $\sim 0.1M_\odot$ is an outcome for $M_{\rm NS} = 1.3M_\odot$ and $R_{\rm NS} = 13$–14 km, and for $M_{\rm BH} = 3$–$4M_\odot$.

In the previous work, we assumed that the NSs were corotating around the center of mass of the system, for simplicity. However, this is not a very realistic velocity field for the NS in close compact binaries [20]. Recently, we have developed a new code for computing quasicircular states of a BH and an irrotational NS. For obtaining the irrotational velocity field of the NS, one has to solve the equation for the velocity potential [21]. We employ the same method as that for computing the NS-NS binaries (e.g., [22,23]), which has been used in our project for the NS-NS merger [16,17]. (For solving the basic equations for the initial data, we use the spectral method library LORENE developed by the Meudon Relativity Group [24].) In addition, we modify our simulation code for the Einstein evolution equation to the fourth-order scheme for more accurate computation. In this paper, we present numerical results of the simulations, employing new quasicircular states as the initial conditions and a new simulation code. Changing the BH mass and NS radius, we systematically investigate the dependence of the torus mass formed after the merger on $M_{\rm BH}$ and $R_{\rm NS}$. We also compute gravitational waveforms during the tidal disruption, and their spectrum.

The paper is organized as follows. Section II summarizes the initial conditions chosen in this paper. Section III briefly describes the formulation and numerical methods for the simulation. Section IV presents the numerical results of the simulation for the merger of BH-NS binaries.

Section V is devoted to a summary. In the following, the geometrical units of $c = G = 1$ are used.

II. INITIAL CONDITION

We compute the initial condition for the numerical simulation by employing a formulation in the moving puncture framework which is described in our previous papers [15]. This formulation is slightly different from that in [3,4,25,26], although both formulations are based on the conformal flatness formulation for the three-metric, and solve the equations of the maximal slicing condition, and Hamiltonian and momentum constraints. (See [27] for the simulations preformed employing the initial data presented in [3]). Although the basic equations adopted in this paper are the same as those described in [15], we slightly change the method for defining the quasicircular state as follows: In the previous paper, we determined the center of mass of the system, imposing that the dipole moment of the conformal factor at spatial infinity is zero. In this paper, the center of mass is determined from the condition that the azimuthal component of the shift vector β^φ at the location of the puncture is equal to $-\Omega$, where Ω is the orbital angular velocity. Namely, we impose the corotating gauge condition at the location of the puncture. The reason for this change is that, with this new method, the curve of the angular momentum J as a function of the orbital angular velocity Ω along quasicircular sequences is closer to the curve derived from the third PN equation of motion [6]: For the same angular velocity, the angular momentum of quasicircular states obtained in the previous method is smaller by $\sim 1\%$ than that in the present case. Furthermore, the relation among the orbital angular velocity, Arnowitt-Deser-Misner (ADM) mass M, and angular momentum agrees with the results obtained by a different method [3,4] fairly well; for the mass ratio and NS radii adopted in this paper, the disagreement of the angular momentum for a given angular velocity is likely to be much smaller than 1%; cf. Fig. 1, which compares the relation between angular momentum and angular velocity (see the caption for details). Because the relation disagrees by $\sim 1\%$ with the third PN relation, our initial condition would contain a slightly spurious eccentricity of several percent [28].

As the velocity field of the NS, we assume the irrotational one because it is believed to be the realistic velocity field [20]. The density profile and velocity field are determined by solving the hydrostatic equation (the first integral of the Euler equation) and an elliptic-type equation for the velocity potential [21].

The NSs are modeled by a polytropic EOS

$$P = \kappa \rho^\Gamma, \tag{6}$$

where P is the pressure, ρ the rest-mass density, κ the polytropic constant, and Γ the adiabatic index for which we set $\Gamma = 2$. κ is a free parameter, and in the following we choose it so as to fix the rest mass of the NSs to be $M_* = 1.4 M_\odot$ because this value is close to the canonical value [1]. We note that the mass, radius, and time can be rescaled arbitrarily by changing κ: i.e., if we change the value of κ from κ_1 to κ_2, these quantities are rescaled systematically by a factor of $(\kappa_2/\kappa_1)^{1/2}$ for $\Gamma = 2$. By contrast, the nondimensional parameters such as $M_{\rm NS}/R_{\rm NS}$, $M\Omega$, $M\kappa^{-1/2}$, $R_{\rm NS}\kappa^{-1/2}$, and mass ratio are invariant. In this paper, we present the results for the specific values of κ to help the general readers who are not familiar with the nondimensional units [29].

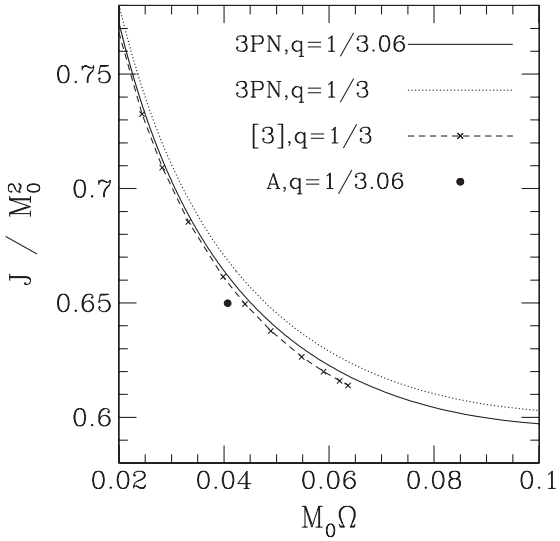

FIG. 1. Angular momentum (J/M_0^2) vs angular velocity ($M_0\Omega$) for model A (filled circle). [For models B and C, which have the same mass ratio as that of model A ($q = M_{\rm NS}/M_{\rm BH} = 1/3.06$), the location of the plots is approximately the same.] For comparison, the relation for the binary of $q = 1/3.06$ in the third PN theory (solid curve) and numerical results of Ref. [3] for $q = 1/3$ are shown together (note that the mass ratio q is slightly different from that of models A–C, and hence the relation for $q = 1/3$ in the third PN theory is plotted together by the dotted curve). Because J/M_0^2 is approximately proportional to the ratio of reduced mass to total mass, the angular momentum for the hypothetical sequence of $q = 1/3.06$ computed by the formulation of Ref. [3] would be by $\approx 1\%$ systematically smaller than those presented in this figure, and would approximately coincide with our results within 1% disagreement.

Because we choose $M_* = 1.4 M_\odot$, the NS mass is in the narrow range $M_{\rm NS} \approx 1.29 M_\odot$–$1.31 M_\odot$ irrespective of the NS radius $R_{\rm NS}$. The NS radius is chosen to be 12.0, 13.2, and 14.7 km. These values agree approximately with those predicted by the nuclear EOSs in which the predicted radii are $R_{\rm NS} \approx 10$–15 km for $M_{\rm NS} = 1.3 M_\odot$ [30]. The value $R_{\rm NS} = 12$ km agrees approximately with that predicted by the stiff nuclear EOSs such as the Akmal-Pandharipande-Ravenhall EOS [31].

The BH mass is chosen in the range $M_{\rm BH} \approx 3.3 M_\odot$–$4.6 M_\odot$. As we described in Sec. I, the tidal disruption of the chosen NSs occurs for such low-mass BHs.

TABLE I. Parameters for the quasicircular states of BH-NS binaries. The mass parameter of the puncture (M_p), the BH mass (M_{BH}), the rest mass of the NS (M_*), the mass (M_{NS}), the circumferential radius (R_{NS}), and the normalized mass ($M_*\kappa^{-1/2}$) of the NS in isolation, the mass ratio (q), the ADM mass of the system (M), the total angular momentum (J), in units of M^2, the orbital period (P_0), in units of $M_0 = M_{BH} + M_{NS}$, and the compactness of the system defined by $(M_0\Omega_0)^{2/3}$, where Ω_0 is the orbital angular velocity. The BH mass is computed from the area of the apparent horizon A as $(A/16\pi)^{1/2}$. $M_0\Omega_0$ is ≈ 0.040–0.041 for models A–F. Models Ab and Ac are data for test simulations (see Sec. IVA).

Model	$M_p(M_\odot)$	$M_{BH}(M_\odot)$	$M_*(M_\odot)$	$M_{NS}(M_\odot)$	R_{NS} (km)	$M_*/\kappa^{1/2}$	q	$M(M_\odot)$	J/M^2	P_0/M_0	$(M_0\Omega_0)^{2/3}$
A	3.906	3.975	1.400	1.302	13.2	0.150	0.327	5.227	0.662	154	0.118
B	3.881	3.950	1.400	1.294	12.0	0.160	0.327	5.193	0.660	154	0.119
C	3.930	4.001	1.400	1.310	14.7	0.140	0.328	5.260	0.663	152	0.119
D	3.255	3.321	1.400	1.302	13.2	0.150	0.392	4.576	0.725	157	0.117
E	3.234	3.300	1.400	1.294	12.0	0.160	0.392	4.546	0.721	154	0.118
F	4.557	4.627	1.400	1.302	13.2	0.150	0.281	5.878	0.612	158	0.117
Ab	3.906	3.981	1.400	1.302	13.2	0.150	0.327	5.230	0.649	138	0.127
Ac	3.906	3.987	1.400	1.302	13.2	0.150	0.327	5.233	0.639	126	0.136

In the present work, we prepare quasicircular states with $M_0\Omega_0 \approx 0.04$, where Ω_0 is the orbital angular velocity of the quasicircular states. With such an initial condition, the BH-NS binary experiences about one-and-half orbits before the onset of merger. In order to reduce the spurious ellipticity and to take into account the nonzero radial velocity associated with the gravitational radiation reaction, we may need to perform a simulation for several orbits before the onset of merger, starting from a more distant orbit [32–34]. In the present paper, however, we focus primarily on the qualitative study of the tidal disruption events. For such purpose, the adopted initial conditions are acceptable (see Appendix B). The simulation of the long-term evolution for the inspiral phase (in particular, for computation of accurate gravitational waveforms) is left for the future. For such a simulation, the adaptive mesh refinement (AMR) algorithm is required, as illustrated in the study of BH-BH merger [32–34]. We plan to perform such simulation in the near future.

In Table I, the parameters of the quasicircular states adopted in this paper are listed. Specifically, we prepare six models (A–F) for clarifying the dependence of the tidal disruption events on the NS radius and mass ratio. The NSs for models A, B, and C and for models D and E, respectively, have approximately the same mass ratio $q = M_{NS}/M_{BH}$, although the NS radii are different from each other. Comparing the numerical results among these models, the dependence of the properties of the tidal disruption event on the NS radius is clarified. The NS radius for models A, D, and F and for models B and E are the same, although the mass ratios are different from each other. Thus, comparison of the numerical results for these models clarifies the dependence of the properties of the tidal disruption event on the mass ratio.

III. NUMERICAL METHODS

The numerical code for the hydrodynamics is the same as that in [15], where we use a high-resolution central scheme with the third-order piecewise parabolic interpolation and with a steep min-mod limiter in which the limiter parameter b is set to 2.5 (see Appendix A of [35]). We have already used this numerical code for the simulation of the NS-NS binary merger [17,36]. We adopt the Γ-law EOS in the simulation as

$$P = (\Gamma - 1)\rho\varepsilon, \tag{7}$$

where ε is the specific internal energy and $\Gamma = 2$.

For solving the Einstein evolution equation, we use the original version of the Baumgarte-Shapiro-Shibata-Nakamura formalism [37]. Namely, we evolve the conformal part of the three-metric, $\phi \equiv (\ln\gamma)/12$, the trace part of the extrinsic curvature, K, the conformal three-metric, $\tilde{\gamma}_{ij} \equiv \gamma^{-1/3}\gamma_{ij}$, the tracefree extrinsic curvature, $\tilde{A}_{ij} \equiv \gamma^{-1/3}(K_{ij} - K\gamma_{ij}/3)$, and a three-auxiliary variable, $F_i \equiv \delta^{jk}\partial_j\tilde{\gamma}_{ik}$. Here, γ_{ij} is the three-metric, K_{ij} the extrinsic curvature, $\gamma \equiv \det(\gamma_{ij})$, and $K \equiv K_{ij}\gamma^{ij}$. In the previous paper [15], we solved the equation for $\gamma^{-1/2}$. Since then, we have learned that we do not have to evolve the inverse of the conformal factor even in the moving puncture framework, because we use the cell-centered grid in which the puncture is never located on the grid points.

For the condition of the lapse function α and the shift vector β^i, we adopt a dynamical gauge condition in the following form:

$$(\partial_t - \beta^i\partial_i)\ln\alpha = -2K, \tag{8}$$

$$\partial_t\beta^i = 0.75\tilde{\gamma}^{ij}(F_j + \Delta t\partial_t F_j). \tag{9}$$

Here, Δt denotes the time step in the simulation, and the second term on the right-hand side of Eq. (9) is introduced for the stabilization of the numerical computation.

The numerical code for solving the Einstein equation is slightly modified from the previous version as follows: (i) All the spatial finite differencing including the advection term such as $\beta^i\partial_i\phi$ is evaluated with the fourth-order

finite-differencing scheme. For the advection term, an upwind method is adopted as proposed, e.g., in [19]. (ii) For the time integration, a third-order Runge-Kutta scheme is employed. With this scheme, the stable evolution is feasible. Furthermore, the numerical accuracy is significantly improved, and as a result, the convergent results can be obtained by a relatively wider grid spacing than by that adopted in the previous papers [15].

The location and properties of the BH, such as the area and circumferential radii, are determined using an apparent horizon finder, for which our method is described in [38].

For extracting gravitational waves from the geometrical variables, the gauge-invariant Moncrief variables R_{lm} in the flat spacetime [39] have been computed in our series of papers (e.g., [16,17,40]). From R_{lm}, the plus and cross modes of gravitational waves, h_+ and $h_\times$, are obtained by a simple algebraic calculation. The detailed equations are described in [16,40], to which the reader may refer. In this method, we split the metric in the wave zone into the flat background and linear perturbation. Then, the linear part is decomposed using the tensor spherical harmonics, and the gauge-invariant variables are constructed for each mode of the eigenvalues (l, m). The gauge-invariant variables of $l \geq 2$ can be regarded as gravitational waves in the wave zone, and hence we derive such modes in the numerical simulation.

In the present work, we also compute the outgoing part of the Newman-Penrose quantity (the so-called ψ_4; see, e.g., [19,32] for the definition of ψ_4). By performing the time integration of $2\psi_4$ twice (and with an appropriate choice of the integration constants), one can compute the gravitational waveforms. We compare these gravitational waveforms with those computed from the gauge-invariant wave-extraction method. It is found that the wave phases of both waveforms agree well from the inspiral phase to the tidal disruption phase. However, the amplitude does not agree well in the early inspiral phase; the magnitude of the disagreement is ~20%–30% (the amplitude by the gauge-invariant variables is always larger), although the disagreement is much smaller during the tidal disruption. The reason is that we extract gravitational waves near the outer boundary, which is located in the local wave zone in the present work, and the amplitude is not the correct asymptotic amplitude. To obtain the asymptotic amplitude, it is necessary to perform the extrapolation using the data of different extraction radii. One point worth noting is that the convergence of the amplitude of $D\psi_4$ for increasing the extraction radius D is much faster than that for DR_{lm}. This indicates that ψ_4 is a better tool than R_{lm} for evaluating the asymptotic waveforms with smaller systematic error, in the simulation where the outer boundary is located in the local wave zone. Hence, we decide that, in this paper, we evaluate the waveform, energy, angular momentum, and linear momentum fluxes by analyzing ψ_4.

We compute the modes of $2 \leq l \leq 4$ for ψ_4, and find that the mode of $(l, |m|) = (2, 2)$ is dominant, but $l = |m| = 3$ and $l = |m| = 4$ modes also contribute to the energy and angular momentum dissipation by more than 1% for the merger of the chosen initial data.

We also estimate the kick velocity from the linear momentum flux of gravitational waves. The linear momentum flux dP_i/dt is computed from the same method as that given in [19,41,42]. Specifically, the coupling terms between $l = |m| = 2$ and $l = |m| = 3$ modes and between $l = |m| = 2$ and $(l, |m|) = (2, 1)$ modes primarily contribute the linear momentum flux. From the total linear momentum dissipated by gravitational waves,

$$\Delta P_i = \int \frac{dP_i}{dt} dt, \tag{10}$$

the kick velocity is defined by $\Delta P_i/M$, where M is the initial ADM mass of the system.

IV. NUMERICAL RESULTS

A. Choosing the grid points

In the simulation, the cell-centered Cartesian, (x, y, z), grid is adopted to avoid the situation that the location of the puncture (which always stays in the $z = 0$ plane) coincides with one of the grid points. The plane symmetry is assumed with respect to the equatorial plane. The computational domain of $-L \leq x \leq L$, $-L \leq y \leq L$, and $0 < z \leq L$ is covered by the grid size of $(2N, 2N, N)$ for x-y-z, where L and N are constants. Following [15,37], we adopt a nonuniform grid as follows: an inner domain of the $(2N_0, 2N_0, N_0)$ grid zone is covered with a uniform grid of spacing Δx, and outside this inner domain, the grid spacing is increased according to the relation $\xi \tanh[(i - N_0)/\Delta i]\Delta x$, where i denotes the ith grid point in each positive direction, and N_0, Δi, and ξ are constants. Then, the location of the ith grid, $x^k(i)$, in each direction is

$$x^k(i) = \begin{cases} (i - 1/2)\Delta x & 1 \leq i \leq N_0 \\ (i - 1/2)\Delta x + \xi \Delta i \Delta x \log[\cosh\{(i - N_0)/\Delta i\}] & i > N_0 \end{cases} \tag{11}$$

and $x^k(-i) = -x^k(i)$, $i = 1, 2, \cdots, N$ for $x^k = x$ and y.

For all the simulations, we chose $N = 225$ and $\Delta i = 30$. For most of the simulations, we determined the grid spacing for the inner uniform domain according to the rule $\Delta x/M_{\rm p} = 1/15$, where $M_{\rm p}$ is the mass parameter of the puncture (which is about 2% smaller than the BH mass in the present case). We have found that, with this choice of grid size, a convergent result for the BH orbit is obtained.

Indeed, the simulations for the BH-BH binary in the moving puncture framework (e.g., [18,19,33]) show that this choice is appropriate for obtaining a convergent result in the fourth-order scheme. By increasing the mass ratio M_p/M_{NS}, however, the grid number for covering the NS becomes small for the fixed value of Δx. We require that the major diameter of the NS, L_{NS}, should be covered by $\gtrsim 50$ grid points, because a result with acceptable error is obtained with such a setting (see below and Appendix A). For this reason, for model F we choose $\Delta x/M_p = 1/16$.

In Table II, we list the parameters for the grid coordinates. λ_0 denotes the wavelength of gravitational waves at $t = 0$ ($\lambda_0 = \pi/\Omega_0$). N_0 is chosen so as to put the NS in the inner uniform-grid domain initially. ξ determines the grid spacing near the outer boundary, which is approximately equal to $\xi\Delta x$. We choose ξ from the following conditions: (i) $L/\lambda_0 \gtrsim 0.75$ and (ii) the grid spacing near the outer boundaries is smaller than $1.05M$. Note that the gravitational wavelength λ decreases with time because the orbital radius decreases due to the gravitational radiation reaction. Hence, L is smaller than λ at the onset of tidal disruption, although L is comparable to λ at the onset of simulations. The gravitational wavelength after the merger sets in is expected to be larger than $11M$, which is approximately equal to the wavelength of the quasinormal mode (QNM) of the BH excited in the final phase of the merger. Because the wavelength is covered by at least 10 grid points, we may expect that gravitational waves are extracted with good accuracy near the outer boundary.

To see the dependence of the numerical results on the grid resolution, we performed test simulations for $\Delta x = M_p/12$ (models A2 and C2), for $\Delta x = M_p/13.5$ (model A1), and for $\Delta x = M_p/16$ (model A0). For models A, A0, A1, and A2 and for models C and C2, the locations of the outer boundaries are approximately the same, respectively (see Table II). We found that the numerical results (see Appendix A) systematically vary with varying the grid resolution, and indicate an acceptable convergence for a qualitative study in the case that the grid spacing satisfies the following conditions: (i) $\Delta x \le M_p/12$ and (ii) the diameter of the NS is covered by more than ≈ 50 grid points. As we discuss in Appendix A, the mass surrounding the BH may be overestimated by a factor of ~ 2 ($+ 0.05M_\odot$ for model A2) even for such a setting, whereas the area of the apparent horizon is underestimated only by $\lesssim 1.5\%$. The total energy and angular momentum emitted by gravitational waves are computed with $\sim 10\%$–20% error.

TABLE II. Parameters for the grid in the numerical simulation. The grid number for covering one positive direction (N), the grid number for the inner uniform-grid domain (N_0), the parameters for the nonuniform-grid domain ((Δi, ξ)), the grid spacing in the uniform domain in units of M_p, the grid number covered for the major diameter of the NS (L_{NS}), and the ratio of the location of the outer boundary along each axis to the gravitational wavelength at $t = 0$ (λ_0) are given. For the initial conditions of models A–F, $\lambda_0 = 77$–$79M_0$.

Model	N	N_0	Δi	ξ	$\Delta x/M_p$	$L_{NS}/\Delta x$	L/λ_0
A	225	150	30	20.5	1/15	55	0.86
B	225	150	30	20.5	1/15	49	0.86
C	225	151	30	20.5	1/15	63	0.86
D	225	155	30	20.5	1/15	67	0.74
E	225	150	30	20.5	1/15	59	0.82
F	225	155	30	22.0	1/16	50	0.80
A0	235	160	30	22.0	1/16	59	0.86
A1	211	136	30	18.35	1/13.5	49	0.86
A2	195	121	30	16.4	1/12	44	0.86
C2	195	121	30	16.2	1/12	50	0.86
Ab	210	140	30	20.5	1/15	55	0.86
Ac	200	130	30	20.5	1/15	55	0.86

In the previous papers [15], we performed simulations in the second-order-accurate finite differencing for solving the Einstein equation. In such a case, the convergence of the numerical results with improving the grid resolution is slow. In the present work, we employ the fourth-order scheme, with which the convergence is achieved much faster. However, the convergence is still not perfect, in particular, for following angular momentum transport during tidal disruption and subsequent torus formation. The torus mass may be systematically overestimated by a factor of 2 in the present results, although such systematic error does not change the conclusion (merger process, qualitative properties of gravitational waves, and order of the torus mass) in this paper. To obtain more convergent results about the torus mass, it is necessary to perform a better-resolved simulation for following angular momentum transport precisely.

We also performed test simulations, preparing initial conditions for which initial orbital angular velocity (orbital separation) is larger (smaller) but the mass and radius of NS and the mass of the BH are the same as those for model A (see models Ab and Ac in Table I). We find that the numerical results, such as gravitational waveforms and merger process, are qualitatively unchanged, although they change quantitatively. One point to be noted is that the torus mass surrounding the BH in the final stage is systematically smaller for larger initial orbital angular velocity. The likely reason is that with too large initial orbital angular velocity, the inspiral time is too short to transport angular momentum inside the NS by the tidal torque. We infer that, for the initial orbital angular velocity with $M_0\Omega_0 \approx 0.04$, the final mass surrounding the BH may be systematically underestimated by a factor of ~ 2, and to obtain the results within the error of $0.01M_\odot$, simulation should be performed employing an initial condition with $M_0\Omega_0 \lesssim 0.03$. Thus, the torus mass presented in the following would be systematically underestimated due to our present choice of initial conditions, although such system-

atic error does not change the conclusion in this paper. We briefly present the results of the test simulations in Appendix B.

B. Atmosphere

Because any conservation scheme of hydrodynamics is unable to evolve a vacuum, we have to introduce an artificial atmosphere outside the NS. However, if the density of the atmosphere were too large, it might affect the orbital motions of the BH and NS, and moreover, we might overestimate the total amount of the rest mass of the formed torus surrounding a BH. Thus, we initially assign a small rest-mass density as follows:

$$\rho = \begin{cases} \rho_{\rm at} & r \le x(N_0), \\ \rho_{\rm at} e^{1-r/x(N_0)} & r > x(N_0). \end{cases} \tag{12}$$

Here, we choose $\rho_{\rm at} = \rho_{\rm max} \times 10^{-8}$, where $\rho_{\rm max}$ is the maximum rest-mass density of the NS. With such a choice,

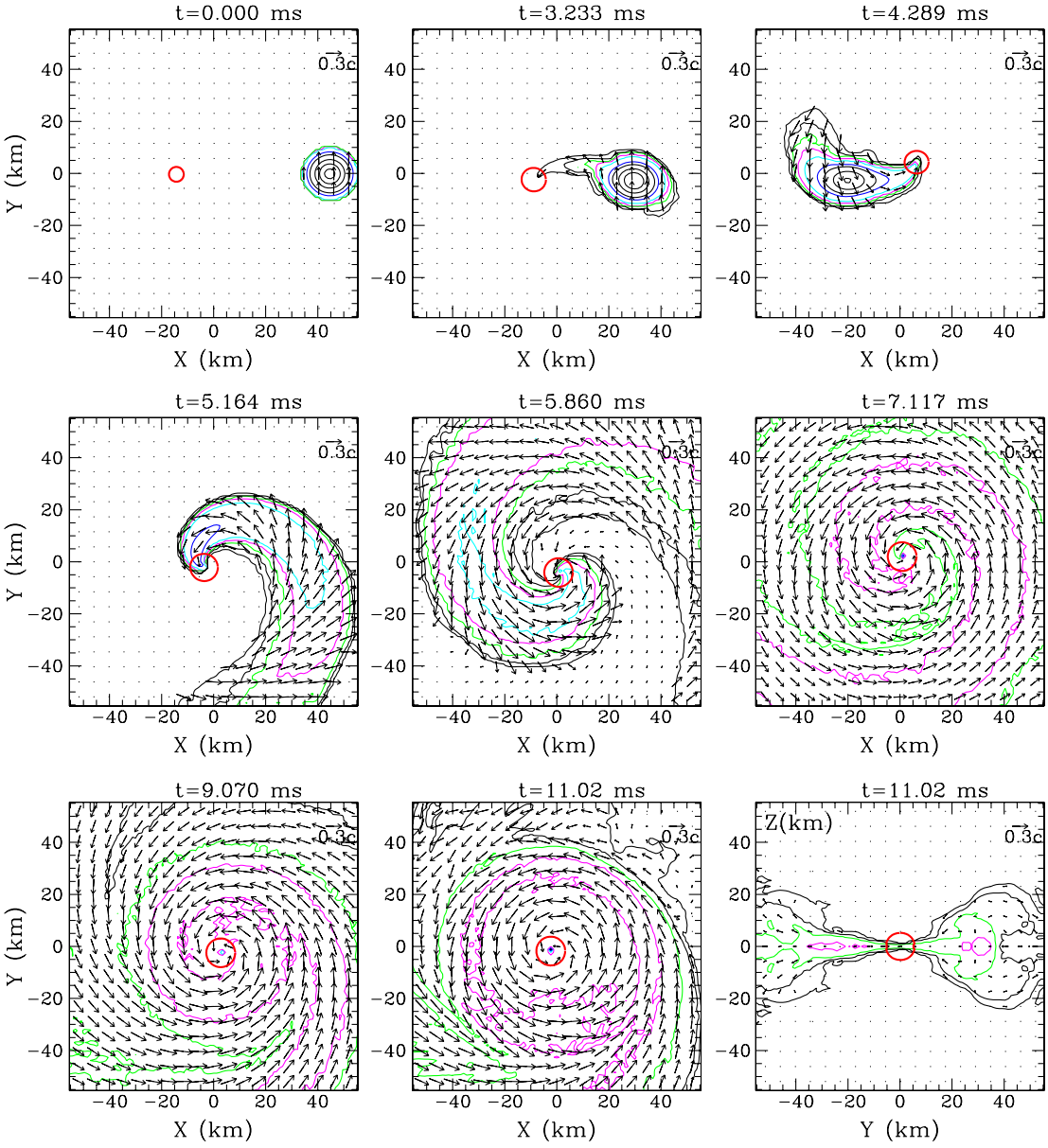

FIG. 2 (color online). Snapshots of the density contour curves for ρ and the three-velocity for $v^i (= dx^i/dt)$ in the equatorial plane for model A. The solid contour curves are drawn for $\rho = 2i \times 10^{14}$ g/cm^3 ($i = 1$–4) and for 10^{14-i} g/cm^3 ($i = 1 \sim 5$). The maximum density at $t = 0$ is $\approx 8.86 \times 10^{14}$ g/cm^3. (The blue, cyan, magenta, and green curves denote 10^{14}, 10^{13}, 10^{12}, and 10^{11} g/cm^3, respectively.) The vectors shows the velocity field (v^x, v^y), and the scale is shown in the upper right-hand corner. The thick (red) circles are the apparent horizons. The second and third panels denote the states after one orbit and one-and-half orbits, respectively. The last panel plots the density contours and velocity vectors in the $x = 0$ plane at the same time as that for the eighth panel.

the total amount of the rest mass of the atmosphere is about 10^{-5} of the rest mass of the NS. Thus, the accretion of the atmosphere onto the NS and BH plays a negligible role for their orbital evolution in the present context. In the following, we discuss the rest mass of the torus surrounding a BH. As we show below, the rest mass is larger than $0.01M_\odot$, which is much larger than the atmosphere's mass. Hence, the atmosphere plays a negligible role for determining the properties of the torus.

C. General process of tidal disruption

All the numerical simulations were performed from about one-and-half orbits before the onset of tidal disruption to the time in which the accretion time scale of material into the BH is much longer than the dynamical time scale. The simulations were performed with no numerical instability. The duration of the simulations is $400M$–$500M$ in units of the ADM mass. In this section, we first describe the general process of tidal disruption, subsequent evolution of the BH, and formation of the accretion disk (torus), showing the numerical results for model A.

Figure 2 plots the evolution of the contour curves for ρ and the velocity vectors for the three-velocity $v^i(=dx^i/dt)$ in the equatorial plane for model A. The locations of the apparent horizons (thick solid circles) are shown together. Because of gravitational radiation reaction, the orbital radius decreases and then the NS is elongated gradually (panels 2 and 3). The tidal disruption of the NS by the BH sets in at $t \sim 4.3$ ms (at about one-and-half orbits; panel 3). Soon after this time, the outer part of the NS expands outward due to angular momentum transport by the hydrodynamic interaction. This material subsequently forms a torus around the BH. However, the tidal disruption sets in at an orbit very close to the ISCO, and hence the material in the inner part is quickly swallowed by the BH (panels 4 and 5). By the outward angular momentum transport, the material in the outer part of the NS forms a one-armed spiral arm (panels 5 and 6). The spiral arm then winds around the BH, and the material, which does not have angular momentum large enough to orbit the BH, shrinks and falls into the BH (panel 7). A relatively large fraction of the material falls, in particular, for $t \approx 9$–11 ms [see also the upper panel of Fig. 6(a)]. In this phase, the inner and outer parts of the spiral arm collide, and thermal energy is generated due to the shock heating. The high-density part of the spiral arm then expands to form a compact torus with the maximum density $\sim 10^{12}$ g/cm^3 (panels 8 and 9; see also Fig. 3). We stopped the simulation at $t \approx 12.5$ ms, at which the rest mass of the material located outside the apparent horizon is $\approx 0.092M_\odot$.

We define the specific thermal energy generated by the shocks by

$$\varepsilon_{\rm th} \equiv \varepsilon - \frac{\kappa}{\Gamma - 1}\rho^\Gamma, \tag{13}$$

where the second term on the right-hand side is the polytropic term, i.e., the specific internal energy in the absence of the shocks. $\varepsilon_{\rm th}$ is zero in the adiabatic evolution (in the absence of the shocks), and hence $\varepsilon_{\rm th}$ may be regarded as the specific thermal energy generated by the shocks. Figure 3 (top panel of each) plots $\varepsilon_{\rm th}$ along the x and y axes at $t = 7.117$, 9.070, and 11.02 ms. The ratio of the thermal energy to the total internal energy $\varepsilon_{\rm th}/\varepsilon$ and the rest-mass density are shown together. This figure shows that the generated thermal energy is much larger than the polytropic one for most regions except for the high-density region of the spiral arms which do not experience the shock heating. However, during the evolution, the spiral arms wind around the BH and the shocked region increases. As a result, $\varepsilon_{\rm th}/\varepsilon$ eventually becomes approximately equal to unity for all the regions. Figure 3 indicates that a hot torus with the density $\sim 10^{11}$–10^{12} g/cm^3 is the final outcome. This is a favorable property for producing a large amount of neutrinos which may drive SGRBs (e.g., [43–46]).

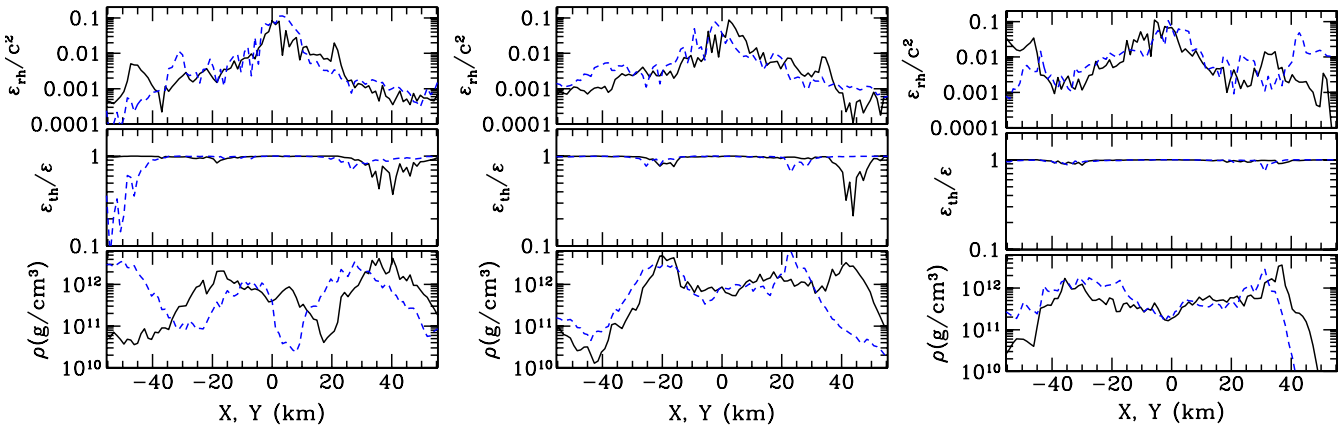

FIG. 3 (color online). Profiles of $\varepsilon_{\rm th}$, $\varepsilon_{\rm th}/\varepsilon$, and ρ along the x axis (solid curves) and y axis (dashed curves) at $t = 7.117$ ms (left), 9.070 ms (middle), and 11.02 (right).

Although the EOS adopted in this paper is an idealized one, we approximately estimate the temperature of the torus. Assuming that the specific thermal energy is composed of those of the gas, photons, and relativistic electrons (and positrons), we have [45,46]

$$\varepsilon_{\rm th} = \frac{3kT}{2m} + \frac{11a_r T^4}{4\rho}, \tag{14}$$

where k, a_r, T, and m are the Boltzmann constant, radiation-density constant, temperature, and mass of the main component of nucleons. For simplicity, we assume that the gas is composed of the neutron and set $m = 1.66 \times 10^{-24}$ g. Because the temperature is higher than $\sim 6 \times 10^9$ K (see below), we assume that the electrons and positrons are relativistic to describe Eq. (14). If the density is high, the neutrinos are optically thick and contribute to the thermal energy. Although this effect is important for $\rho \gtrsim 10^{12}$ g/cm^3 [43–46], the density of the outcome is at most 10^{12} g/cm^3, and hence it is safely ignored. Then, the radiation energy is smaller than the gas energy for $\rho \gtrsim 10^{11}$ g/cm^3 and $\varepsilon_{\rm th}/c^2 \lesssim 0.01$. From Eq. (14), the temperature is approximately given by

$$T \approx 7.2 \times 10^{10} \left(\frac{\varepsilon_{\rm th}}{0.01}\right) \text{K}. \tag{15}$$

Thus, the estimated temperature is between 10^{10} and $\sim 10^{11}$ K for the torus. (Note that $\varepsilon \sim 0.1$ inside the apparent horizon, but we do not pay attention to the inside of the BH.)

For clarification of the dependence of the density and the thermal energy on the radius of the tidally disrupted NSs, $R_{\rm NS}$, we show the same plots as Fig. 3 for models B and C in Fig. 4. We also plot the density contour curves and velocity vectors at $t = 11.02$ ms for these models in Fig. 5. Figure 4 shows that the value of $\varepsilon_{\rm th}$ increases above 0.001, dominating the specific thermal energy irrespective of models. Figure 5 shows that, irrespective of the models, the outcome after the tidal disruption is a compact torus surrounding the BH. Thus, the hot torus is the universal outcome irrespective of $R_{\rm NS}$ as long as it is in the range between 12 and 15 km.

By contrast, the rest-mass density depends sensitively on the torus mass (see Table III and the next section for the final values of the rest mass of the material located outside the apparent horizon, which is approximately equal to the torus mass). For model B, the torus mass is much smaller than that for model A. This is simply because the NS radius is smaller, and hence the tidal disruption sets in at an orbit very close to the ISCO. For model C, by contrast, the torus mass is much larger than those for models A and B because of the larger NS radius. The averaged rest-mass density has a clear correlation with the torus mass. For model B, the density is smaller than 10^{12} g/cm^3 for most regions of the torus, whereas for model C, the density is larger than 10^{12} g/cm^3 for most regions. For such a high-density case, the neutrinos are likely to be optically thick [43], and the neutrino-dominated accretion flow will be subsequently formed.

D. Torus mass

The upper panels of Figs. 6(a)–6(c) plot the evolution of the fraction of the rest mass of the material located outside the apparent horizon $M_{r>r_{\rm AH}}$ (a) for models A, D, and F, (b) for models B and E, and (c) for models A–C. Here, $M_{r>r_{\rm AH}}$ is defined by

$$M_{r>r_{\rm AH}} \equiv \int_{r>r_{\rm AH}} \rho \alpha u^t \sqrt{\gamma} d^3x, \tag{16}$$

and u^t is the time component of the four-velocity. We find

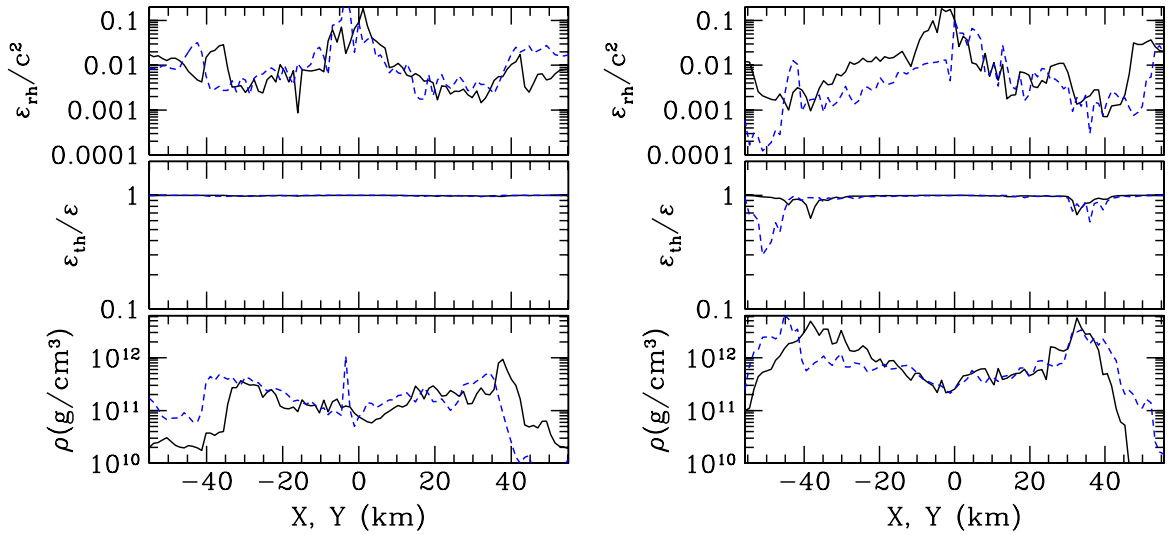

FIG. 4 (color online). Profiles of $\varepsilon_{\rm th}$, $\varepsilon_{\rm th}/\varepsilon$, and ρ along the x axis (solid curves) and y axis (dashed curves) at $t = 11.02$ for models B (left panel) and C (right panel).

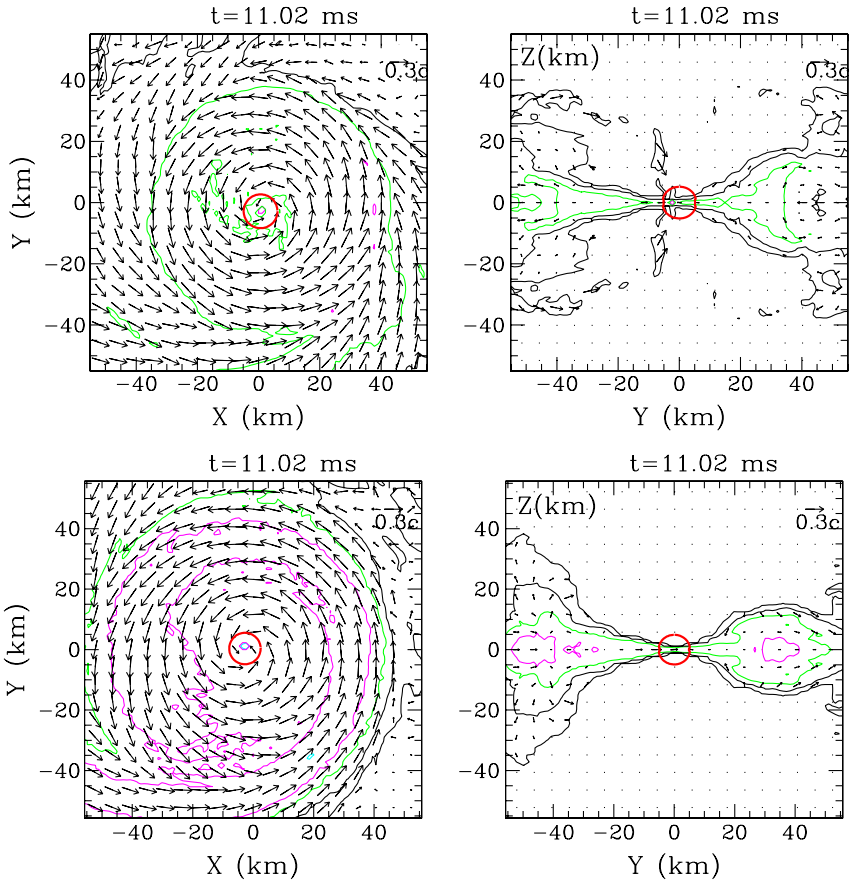

FIG. 5 (color online). The same as Fig. 1 but for models B and C at $t = 11.02$ ms. The upper two panels plot the contour plots and velocity vectors for the x-y and y-z planes for model B. The lower two panels show the plots for model C.

that a large fraction of the material is swallowed by the BH soon after the onset of merger, irrespective of the models (see also Table III). However, the final value of $M_{r>r_{\rm AH}}$ depends strongly on the NS radius; e.g., for $R_{\rm NS} = 14.7$ km and $q \approx 0.33$ (model C), $\approx 12\%$ of the material is located outside the BH at the end of the simulation, whereas for $R_{\rm NS} = 12.0$ km and $q \approx 0.33$ (model B), only $\approx 2\%$ of the material is located outside the BH at the end of the simulation [see Fig. 6(c)]. The final value of $M_{r>r_{\rm AH}}$ depends also on the mass ratio q. Figure 6(a) illustrates that the final value of $M_{r>r_{\rm AH}}$ increases by $\sim 75\%$ for the increase of the value of q from 0.28 to 0.39. Figure 6(b)

TABLE III. The total radiated energy in units of the initial ADM mass M, the total radiated angular momentum in units of the initial angular momentum J, the kick velocity, the rest mass of the material located outside the apparent horizon, the estimated BH mass, the area of the apparent horizon in units of $16\pi M_{\rm BH,f}^2$, the ratio of the polar circumferential radius to the equatorial one of the apparent horizon (C_p/C_e), and the estimated spin parameters of the final state of the BH. $a_{\rm f1}$, $a_{\rm f2}$, and $a_{\rm f3}$ are computed from the area of the apparent horizon, the estimated angular momentum and mass of the BH, and C_p/C_e, respectively. All the values presented here are measured for the states obtained at the end of the simulations. We note that C_p/C_e varies with time by $\approx 0.05\%$. The energy, angular momentum, and linear momentum fluxes of gravitational waves are evaluated changing the location of the extraction, and we found that the energy and angular momentum fluxes converge within $\sim 1\%$ error, whereas the error of the linear momentum flux is $\sim 10\%$. $M_{r>r_{\rm AH}}$ may be overestimated systematically by a factor of ~ 2 (see Sec. IV D and Appendix A).

Model	$\Delta E/M$	$\Delta J/J$	$V_{\rm kick}$ (km)	$M_{r>r_{\rm AH}}(M_\odot)$	$M_{\rm BH,f}(M_\odot)$	$\hat{A}_{\rm AH}$	C_p/C_e	$a_{\rm f1}$	$a_{\rm f2}$	$a_{\rm f3}$
A	0.68%	11.3%	19	0.092	5.099	0.9175	0.9391	0.550	0.560	0.545
B	0.96%	12.9%	13	0.027	5.116	0.9110	0.9350	0.570	0.577	0.561
C	0.45%	8.7%	18	0.159	5.078	0.9241	0.9437	0.530	0.543	0.526
D	0.61%	10.3%	17	0.106	4.442	0.8994	0.9260	0.597	0.612	0.595
E	0.93%	13.0%	19	0.046	4.458	0.8953	0.9220	0.612	0.622	0.608
F	0.77%	12.5%	4	0.060	5.773	0.9288	0.9477	0.514	0.525	0.508

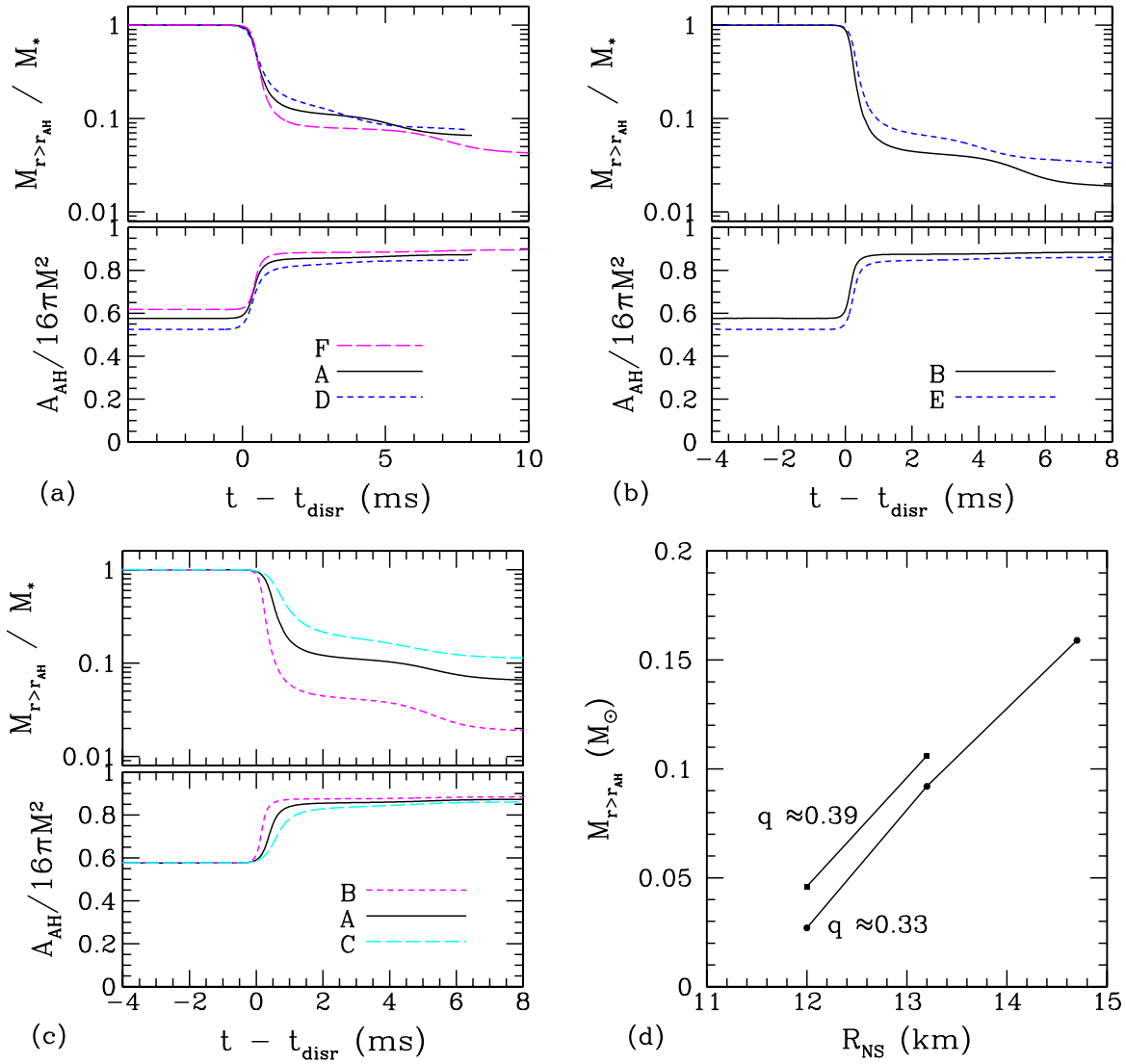

FIG. 6 (color online). The evolution of the rest mass of the material located outside the apparent horizon (upper panel of each figure) and the evolution of the area of the apparent horizon in units of $16\pi M^2$ (lower panel of each figure) (a) for models A, D, and F (for $R_{\rm NS} = 13.2$ km), (b) for models B and E (for $R_{\rm NS} = 12$ km), and (c) for models A, B, and C (for $q \approx 0.33$). $t_{\rm disr}$ in the horizontal axis denotes the approximate time at which the tidal disruption sets in, and we determine it to be 4.5 ms for model A, 4.2 ms for model B, 4.3 ms for model C, 4.2 ms for model D, 3.9 ms for model E, and 5.6 ms for model F, respectively. (d) $M_{r>r_{\rm AH}}$ at the end of the simulations as a function of $R_{\rm NS}$.

also illustrates that the final value of $M_{r>r_{\rm AH}}$ increases by $\sim$50% for the small increase of q from 0.33 to 0.39.

Figures 6(b) and 6(c) [in particular, (c)] clarify the dependence of the infall process of the tidally disrupted material into the BH on the NS radius. With the decrease of the NS radii, the accretion rate of the rest mass into the BH at the onset of tidal disruption increases steeply. Furthermore, the accretion time scale shortens; e.g., for model B, the duration of the quick accretion is shorter than 1 ms, whereas for model C, it is $\sim$1.5 ms.

Figure 6(d) plots the values of $M_{r>r_{\rm AH}}$ at the end of the simulations as a function of $R_{\rm NS}$ for given values of the mass ratio q. It is clearly seen that the fraction of the material located outside the BH steeply decreases with the decrease of the NS radius. Extrapolating the results for the smaller values of $R_{\rm NS}$, we expect that $M_{r>r_{\rm AH}}$ would become close to zero for $R_{\rm NS} \lesssim 11$ km, both for $q = 0.33$ and 0.39. For such a case, a very small value of the BH mass as $M_{\rm BH} < 3M_\odot$ would be required for the formation of a torus of mass $\gtrsim 0.01M_\odot$.

Before closing this section, we remark the following. As we already mentioned in Sec. IV A, systematic error for the estimation of torus mass associated with the insufficient grid resolution and with the large initial orbital angular velocity may be a factor of $\sim$2 in the present results. Because the error is systematic, we believe that the quali-

tative properties of the torus mass, such as its dependence on the NS radius and mass ratio, are not changed even in a simulation with better accuracy and with smaller initial orbital angular velocity. However, for determining the torus mass more precisely, it is necessary to perform a simulation with an improved setting.

E. Black hole mass and spin

The lower panels of Figs. 6(a)–6(c) plot the evolution of the area of the apparent horizon in units of $16\pi M^2$. The area of the BHs is kept to be approximately constant before the onset of tidal disruption. The value of the area fluctuates only by ~0.03% in such a phase. After the onset of tidal disruption, the area quickly increases as a result of the mass accretion, and finally approaches an approximate constant. From the final values of the area of the apparent horizon together with the estimated BH mass at the final stage, $M_{\rm BH,f}$, the nondimensional spin parameter of the formed BHs, a, is approximately derived from

$$\hat{A} \equiv \frac{A}{16\pi M_{\rm BH,f}^2} = \frac{1+\sqrt{1-a^2}}{2}. \tag{17}$$

To approximately estimate $M_{\rm BH,f}$, we use the following equation as in [15]:

$$M_{\rm BH,f} \equiv M - M_{r>r_{\rm AH}} - E_{\rm GW}, \tag{18}$$

where $E_{\rm GW}$ is the total radiated energy by gravitational waves [47]. The results for $E_{\rm GW}$, $M_{r>r_{\rm AH}}$, $M_{\rm BH,f}$, and $\hat{A}$ are listed in Table III. The gravitational wave energy is primarily carried by the $l = |m| = 2$ modes. We found that $l = |m| = 3$ and $l = |m| = 4$ modes are subdominant modes; for $q \approx 0.33$ (0.39), the total emitted energies carried by $l = |m| = 3$ and $l = |m| = 4$ modes are ~5%–6% (4%) and ~1%–2% (1%) of that of $l = |m| = 2$ modes, respectively.

The nondimensional spin parameter determined from $\hat{A}$ is listed in Table III as $a_{\rm f1}$. We find that $a_{\rm f1}$ is between ~0.5 and ~0.6 for all the models, implying that rotating BHs of moderate magnitude of the spin are the final outcomes. For the larger mass ratio q, the spin parameter is larger for the same NS radius. The reason for this is that, for the larger mass ratio, the initial total angular momentum of the system J is larger (see Table I). For the smaller NS radius, the spin parameter is larger for the same mass ratio. This is simply because the larger fraction of the material falls into the BH, resulting in the spin-up.

To check the validity of the above estimate, we evaluate the nondimensional spin parameter employing the other two methods by which the BH spin may be approximately calculated. In the first method, the spin is evaluated directly from the angular momentum of the BH, defined by

$$J_{\rm BH,f} \equiv J - J_{r>r_{\rm AH}} - J_{\rm GW}, \tag{19}$$

where $J_{\rm GW}$ is the total radiated angular momentum by gravitational waves and $J_{r>r_{\rm AH}}$ is the angular momentum of the material located outside the apparent horizon, which is defined by

$$J_{r>r_{\rm AH}} \equiv \int_{r>r_{\rm AH}} \rho \alpha h u^t u_\varphi \sqrt{\gamma} d^3x. \tag{20}$$

Here, u_φ is the φ component of the four-velocity, and h is the specific enthalpy defined by $1 + \varepsilon + P/\rho$. $J_{\rm BH,f}$ exactly gives the angular momentum of the material in the axisymmetric and stationary spacetime. In the late phase of the merger, the spacetime relaxes to a quasistationary and nearly axisymmetric state. Thus, we may expect that $J_{r>r_{\rm AH}}$ will provide an approximate magnitude of the angular momentum of the torus.

From $J_{\rm BH,f}$ and $M_{\rm BH,f}$, we define the nondimensional spin parameter by $a_{\rm f2} \equiv J_{\rm BH,f}/M_{\rm BH,f}^2$ (see Table III). It is found that $a_{\rm f2}$ is systematically larger than $a_{\rm f1}$, but these two values, independently determined, still agree within $\approx$ 2.5% error. This suggests that both quantities denote the BH spin within the error of ~2.5% ($\Delta a \sim 0.015$). We note that because the relation $a_{\rm f1} < a_{\rm f2}$ holds systematically, this disagreement would primarily result from the systematic error associated with the approximate definitions of the spin. For example, we use the rest mass $M_{r>r_{\rm AH}}$ to estimate the torus mass in Eq. (18), ignoring the gravitational binding energy between the BH and the torus. Also, Eq. (20) may include an error because the torus is neither exactly axisymmetric nor stationary.

In the second method, we use the ratio of the polar circumferential length to the equatorial one of the BH, C_p/C_e. We compare this ratio to that of the Kerr BH, and estimate the spin parameter. The results are listed in Table III as $a_{\rm f3}$. Again we find that this agrees with the other two with a good accuracy (within ~1.5% disagreement with $a_{\rm f1}$). We note that the axial ratio varies with time by ~0.05%. This implies that the error for the estimation of $a_{\rm f3}$ is ~0.5% for $a_{\rm f3} = 0.5$–0.6. We also note that the relation between C_p/C_e and the spin parameter in the presence of the torus is slightly different from that of the Kerr BH [48]. However, the systematic error is negligible because the torus mass is only $\lesssim$ 3% of the BH mass.

From these results, we conclude that the spin parameters obtained by three different methods agree within ~2.5% error. We note that all three methods can only approximately determine the spin, and the systematic error associated with their definition should be included. Indeed, the systematic relation $a_{\rm f2} > a_{\rm f1} > a_{\rm f3}$ holds. Hence, the error of ~2.5% results not only from the numerical error but also from the systematic error.

The spin parameter of the formed BHs is smaller than the initial value of J/M^2 of the system by 14%–20%. The primary reason for this in the case that most of the NS matter falls into the BH, i.e., for $R_{\rm NS} = 12$ km, is that gravitational waves carry away the angular momentum by ~13% of J (see Table II). By contrast, for the case

that $M_{r>r_{\rm AH}}$ is large, the angular momentum of the torus occupies a large fraction of J; e.g., for model C, in which $M_{r>r_{\rm AH}} \approx 0.16 M_\odot$, $J_{r>r_{\rm AH}}$ is about 15% of J. In such a case, the angular momentum of the torus is about twice as large as that carried by gravitational waves.

In the case of merger between nonspinning BHs, the final spin parameter is ≈ 0.50, 0.53, and 0.57 for mass ratios $q = 1/3.56$, $1/3.06$, and $1/2.55$, respectively [41]. These values are only slightly smaller than those for the BH-NS merger of the corresponding mass ratio, and the difference is within ~ 0.05. In some cases (e.g. for model C), the spin parameters agree well. However, this is a coincidence due to the following reasons. (i) In the BH-BH merger, gravitational waves are most efficiently emitted in the final merger stage (e.g., [33,34]), whereas in the BH-NS merger, the amplitude of gravitational waves quickly damps during tidal disruption, and so the fraction of emitted gravitational waves in the merger phase is small (see Sec. IV F). Hence, gravitational waves carry away more angular momentum in the BH-BH merger before reaching the final state of the merged BH. (ii) Although the angular momentum carried away by gravitational waves in the BH-NS merger is not as large as in the BH-BH merger, the angular momentum distributed to the torus surrounding the BH is not negligible, as mentioned above. This effect significantly reduces the angular momentum of the final state of the BH. Thus, the mechanisms for determining the final BH spin are different in the BH-BH and BH-NS cases.

F. Gravitational waves

Figures 7(a) and 7(b) plot gravitational waveforms observed along the z axis as a function of the retarded time for model A. The retarded time is approximately defined by

$$t_{\rm ret} \equiv t - D - 2M \ln(D/M), \tag{21}$$

where D is the distance to the observer. The upper panel of Fig. 7(a) plots $+$ and $\times$ modes of gravitational waves, and the lower one plots the Newman-Penrose quantity. The gravitational waveforms are obtained by performing the time integration of the Newman-Penrose quantity twice. Because the $l = |m| = 2$ mode is dominant in the observation along the z axis, we determine the waveforms only from this mode.

From the values of h_+ and $h_\times$, the amplitude of gravitational waves at a distance D is evaluated,

$$h_{\rm gw} \approx 5.0 \times 10^{-22} \left(\frac{\sqrt{h_+^2 + h_\times^2}}{0.2}\right)\left(\frac{100{\rm Mpc}}{D}\right)\left(\frac{M_0}{5.2 M_\odot}\right). \tag{22}$$

Figure 7(a) implies that the maximum amplitude at a distance of $D = 100$ Mpc is $\approx 4 \times 10^{-22}$ for model A.

For $t_{\rm ret} \lesssim 4.5$ ms, the inspiral waveforms are seen: The amplitude increases, and the characteristic wavelength decreases with time. The wavelength at the last inspiral orbit is ~ 0.8 ms, indicating that the orbital period at which the NS is completely disrupted is ~ 1.6 ms; i.e., the angular velocity is $\sim 0.10 M^{-1}$. This value coincides approximately with that of the ISCO, but does not agree with Ω calculated from Eq. (4) (see Sec. I for discussion). This indicates that the tidal disruption may set in approximately at the orbit predicted by the study of the quasicircular orbits, but the NS is completely disrupted near the ISCO.

For 4.5 ms $\lesssim t_{\rm ret} \lesssim 5.5$ ms, the amplitude of gravitational waves decreases quickly. In this phase, the tidal disruption and resultant quick accretion of the material into the BH proceed (see Fig. 6). Thus, gravitational waves could be emitted both by the matter motion and by the QNM oscillation of the BH. The characteristic oscillation period in this phase is ≈ 2.9 kHz. This value is slightly smaller than the value predicted from the perturbation study for the fundamental QNM of BH mass $M_{\rm BH,f} \approx 5.10 M_\odot$ and spin $a = 0.55$. Here, the perturbation study predicts the frequency and damping time scale as [49]

$$f_{\rm QNM} \approx 3.23 \left(\frac{M_{\rm BH,f}}{10 M_\odot}\right)^{-1} [1 - 0.63(1-a)^{0.3}] \ {\rm kHz}, \tag{23}$$

$$t_d \approx \frac{2(1-a)^{-0.45}}{\pi f}, \tag{24}$$

which gives $f_{\rm QNM} \approx 3.19$ kHz. This indicates that gravitational waves are primarily emitted by the matter motion in this phase; the damping of the amplitude is not due to the QNM damping but to the fact that the compactness and degree of nonaxial symmetry of the matter distribution decrease by the tidal disruption.

For $t \gtrsim 5.5$ ms, the rapid accretion stops and the BH approaches a nearly stationary state [see Fig. 6(a)]. Hence, for $t_{\rm ret} \gtrsim 5.5$ ms, the ring-down waveforms of the QNM should be seen. Because gravitational waves are also emitted by the matter moving around the BH, the waveforms are modulated, and the waveforms associated only with the QNM are not clearly seen. However, ψ_4 with 5.4 ms $\lesssim t_{\rm ret} \lesssim 6$ ms can be fitted by the damping waveforms of the fundamental QNM fairly well. Figure 7(b) plots the $l = |m| = 2$ mode of ψ_4 and a fitted waveform as

$$A e^{-t/t_d} \sin(2\pi f_{\rm QNM} t + \delta), \tag{25}$$

where A and δ are constants. For the fitting, we choose the BH mass and spin as $5.10 M_\odot$ and $a = 0.55$. In this case, $f_{\rm QNM} = 3.19$ kHz and $t_d = 0.286$ ms, respectively [49]. This figure shows that gravitational waves are primarily characterized by the fundamental QNM, and the gravitational wave amplitude of the QNM is much smaller than that at the last inspiral orbit. The possible reason for this small amplitude is that the QNM is excited only incoher-

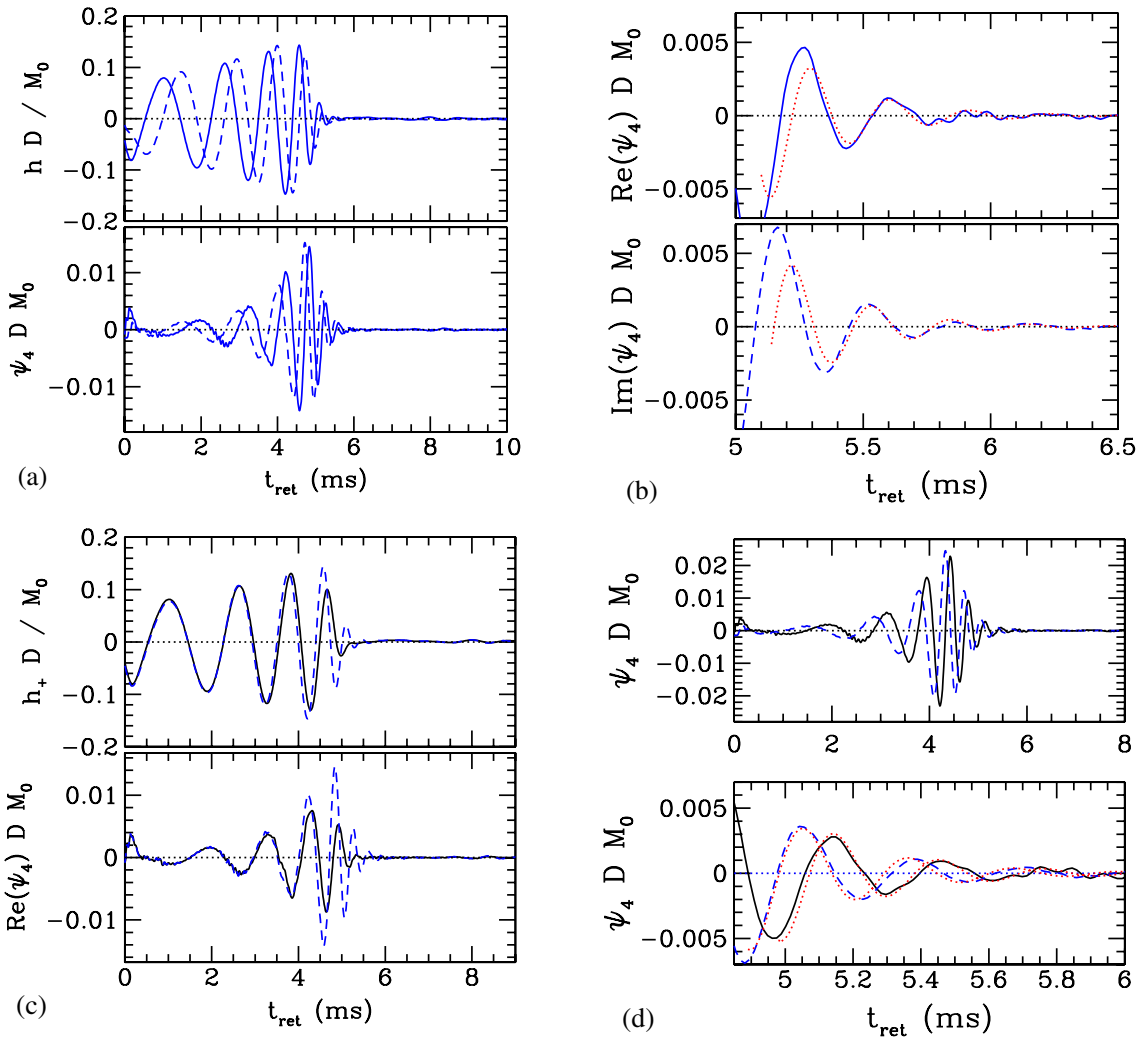

FIG. 7 (color online). (a) Upper panel: + and × modes of gravitational waveforms observed along the z axis for model A (solid and dashed curves, respectively). $t_{\rm ret}$ denotes the retarded time [see Eq. (21)] and M_0 is the total mass defined in the caption of Table I. The amplitude at a distance of observer can be found from Eq. (22). (a) Lower panel: The real and imaginary parts of ψ_4 (solid and dashed curves). (b) The real (upper panel) and imaginary (lower panel) parts of ψ_4 for model A together with the hypothetical curves of gravitational waves associated with the QNM (dotted curves) for 5 ms $\lesssim t_{\rm ret} \lesssim$ 6.5 ms. (c) h_+ (upper panel) and Re(ψ_4) (lower panel) for models A (dashed curve) and C (solid curve). (d) The real (solid curve) and imaginary (dashed curve) parts of ψ_4 for model B (upper panel). The waveforms for 4.8 ms $\lesssim t_{\rm ret} \lesssim$ 6 ms are magnified in the lower panel together with the hypothetical curves of gravitational waves associated with the QNM (dotted curves). For all the plots, only the $l = |m| = 2$ modes are taken into account.

ently by the infall of the tidally disrupted, noncompact material into the BH.

The characteristic feature of the gravitational waveforms emitted after the tidal disruption sets in is that the amplitude damps quickly even in the formation of the nonstationary torus of mass $\sim 0.1 M_\odot$. This is due to the fact that the compactness and degree of nonaxisymmetry of the torus decrease in a very short time scale ($\sim$ 2–3 ms). Moreover, the gravitational wave amplitude of the QNM is very small. This implies that the amplitude of the Fourier spectrum steeply decreases in the high-frequency region for $f \gtrsim 1/0.8$ ms $\approx$ 1.2 kHz (see Sec. IV G; cf. Fig. 8).

Gravitational waveforms are qualitatively similar for other models. However, quantitative differences due to the difference of the NS radius are clearly seen. Figure 7(c) plots gravitational waves for model C (solid curves) together with those for model A (dashed curves). For $t_{\rm ret} \lesssim 4$ ms, the inspiral waveforms for two models agree very well, because gravitational waves at such a phase are primarily determined by the total mass and mass ratio. However, for $t_{\rm ret} \gtrsim 4$ ms, the waveforms disagree because the amplitude for model C starts decreasing (compare the waveforms for 4.5 ms $\lesssim t_{\rm ret} \lesssim$ 6 ms). This earlier decrease results from the onset of tidal disruption of the NS at a larger orbital separation due to the larger NS radius for model C [see Eq. (4)]. Soon after the onset of tidal disruption, the material spreads around the BH at a relatively large orbital separation. Because the compact-

ness and degree of nonaxisymmetry decrease as the tidally disrupted material spreads, the amplitude for model C quickly damps. Furthermore, the fraction of the material coherently falling into the BH is not large. As a result, the amplitude of the QNM is negligible (compare ψ_4 of models A and C; because it is smaller than the amplitude of the wave modulation due to numerical error or matter motion, we cannot extract the QNM for model C).

By contrast, the QNM is clearly seen for the case that the NS radius is smaller. Figure 7(d) plots the $l = |m| = 2$ mode of ψ_4 for model B. In this case, the tidal disruption sets in at an orbit closer to the ISCO than that for models A and C. Consequently, a larger fraction of the material coherently falls into the BH, and relatively coherently excites the QNM. In the lower panel of Fig. 7(d), we again fit the waveforms by Eq. (25) with $f_{\rm QNM} = 3.23$ kHz and $t_d = 0.289$ ms, assuming that the BH mass and spin are $5.12M_\odot$ and 0.57, respectively. Figure 7(d) shows that the waveforms for $t_{\rm ret} \gtrsim 5$ ms agree well with the hypothetical fitting formula. A distinguishable feature is that the amplitude of the QNM is by a factor of $\sim$2 larger than that for model A. However, this amplitude is still much smaller than the amplitude at the last inspiral orbit.

The kick velocity is also estimated from the total linear momentum carried by gravitational waves. We find that it is $\lesssim 20$ km/s for all the models (see Table III) [50]. This value is much smaller (by 1 order of magnitude) than that in the case of the BH-BH merger [41,42,51]. The reason for this is that the gravitational wave amplitude damps quickly during the merger due to the tidal disruption, and the amplitude associated with the QNM is very small. Indeed, a PN study [52] illustrates that the kick velocity is ≈ 20 km/s for $q = 1/3$ if only the kick by gravitational waves from the inspiral motion is taken into account. This value agrees fairly well with our results. In the BH-BH merger, gravitational waves associated with the QNM have a large amplitude, and as a result, the linear momentum flux is significantly enhanced. If the NS escapes the tidal disruption during the merger (i.e., for the case that the BH mass is large enough or the NS radius is small enough), a large kick velocity of order 100 km/s might be induced.

G. Gravitational wave spectrum

To determine the characteristic frequency of gravitational waves emitted during the tidal disruption, we compute the Fourier spectrum of gravitational waves of $l = |m| = 2$ modes defined by

$$h(f) \equiv \frac{D}{M_0}\sqrt{\frac{|h_+(f)|^2 + |h_\times(f)|^2}{2}}, \tag{26}$$

where

$$h_+(f) = \int e^{2\pi i f t} h_+(t) dt, \tag{27}$$

$$h_\times(f) = \int e^{2\pi i f t} h_\times(t) dt. \tag{28}$$

In the present simulations, we followed the inspiral phase only for about one-and-half orbits before the onset of tidal disruption. Thus, the Fourier spectrum for the low-frequency region is absent if we perform the Fourier transformation for the purely numerical data [see the dashed curve of Fig. 8(a)]. To artificially compensate the Fourier spectrum for the low-frequency region, we combine the hypothetical waveforms computed from the third PN approximation for two structureless, inspiraling compact objects [6]. Specifically we determine the evolution of the orbital angular velocity Ω using the so-called Taylor T4 formula (see e.g. [34] for a detailed review) by solving

$$\begin{aligned}\frac{dX}{dt} = \frac{64\eta X^5}{5M_0}\Bigg[& 1 - \frac{743 + 924\eta}{336} X + 4\pi X^{3/2} \\ & + \left(\frac{34\,103}{18\,144} + \frac{13\,661\eta}{2016} + \frac{59\eta^2}{18}\right) X^2 \\ & - \frac{4159 + 15\,876\eta}{672}\pi X^{5/2} + \Bigg\{\frac{16\,447\,322\,263}{139\,708\,800} \\ & - \frac{1712\gamma_E}{105} + \frac{16\pi^2}{3} + \left(\frac{-56\,198\,689}{217\,728} + \frac{451}{48}\pi^2\right)\eta \\ & + \frac{541}{896}\eta^2 - \frac{5605}{2592}\eta^3 - \frac{856}{105}\log(16X)\Bigg\} X^3 \\ & + \left(\frac{-4415}{4032} + \frac{358\,675}{6048}\eta + \frac{91\,495}{1512}\eta^2\right)\pi X^{7/2}\Bigg], \end{aligned} \tag{29}$$

where $X = [M_0\Omega(t)]^{2/3}$ is a function of time, η is the ratio of the reduced mass to the total mass M_0, and $\gamma_E = 0.577\cdots$ is the Euler constant. Then, gravitational waveforms are determined from

$$h_+(t) = \frac{4\eta M_0 X}{D} A(X)\cos[\Phi(t) + \delta], \tag{30}$$

$$h_\times(t) = \frac{4\eta M_0 X}{D} A(X)\sin[\Phi(t) + \delta], \tag{31}$$

where $A(X)$ is a nondimensional function of X for which $A(X) \to 1$ for $X \to 0$, δ is an arbitrary phase, and

$$\Phi(t) = 2\int \Omega(t) dt. \tag{32}$$

For $A(X)$, we choose the 2.5 PN formula (e.g., [34]). The PN waveforms are calculated for $M_0\Omega \geq 0.005$.

In this method, it is not clear at which frequency we should combine the PN waveforms with the numerical waveforms. In the present paper, we match the two waveforms at $M_0\Omega \approx 0.04$ [at $f \approx 517(M_0/5M_\odot)^{-1}$ Hz]. The Fourier spectrum for the late inspiral phase depends on this matching frequency, in particular, around the matching frequency $\sim$500–700 Hz. However, the spectrum around the frequency for $f \gtrsim f_{\rm tidal}$, for which the tidal disruption proceeds, depends very weakly on the matching frequency.

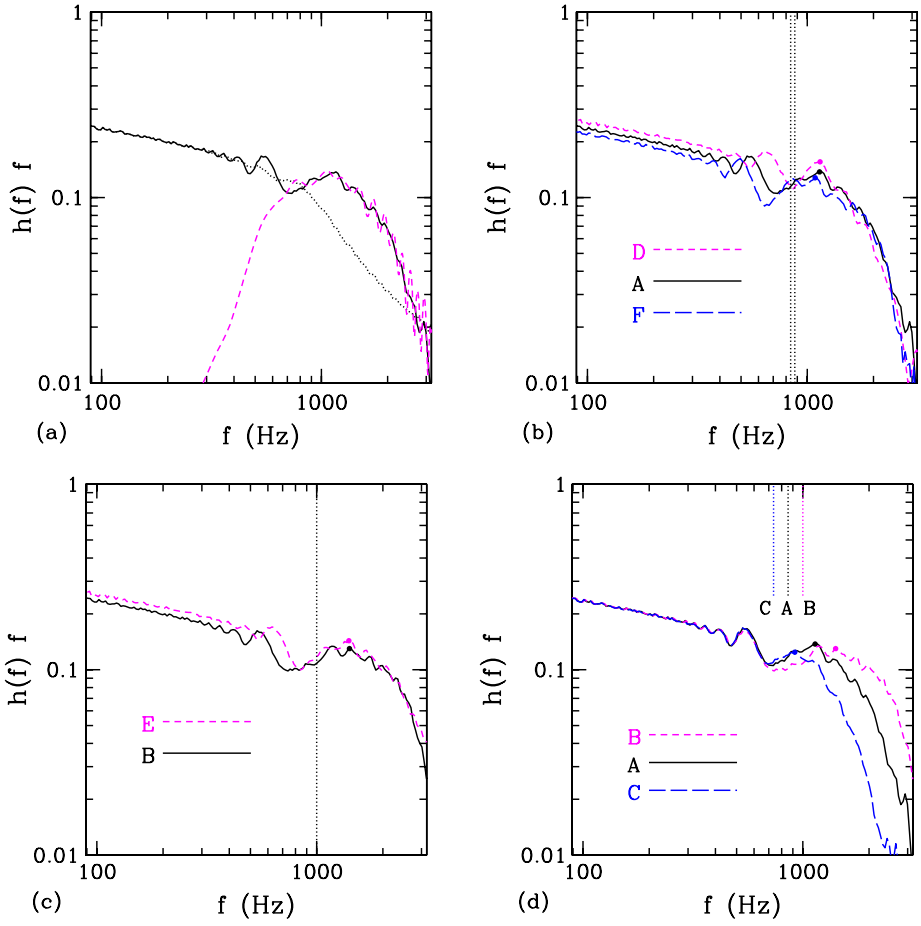

FIG. 8 (color online). (a) Spectrum of gravitational waves $h(f)f$ for model A (solid curve). The dashed and dotted curves are the spectra for the purely numerical (short-term) data and for the analytic third PN waveform. (b) The same as (a) but for models A, D, and F. The vertical dotted lines denote the expected frequencies at which the tidal disruption sets in for models D and F; $f_{\rm tidal} \approx 0.84$ kHz for model F and 0.88 kHz for model D. (c) The same as (b) but for models D and E. The vertical dotted line denotes the expected frequency at which the tidal disruption sets in, $f_{\rm tidal} \approx 1.0$ kHz. (d) The same as (b) but for models A–C. For (b)–(d), the solid circles denote the location of $f_{\rm cut}$.

Thus, the present method is acceptable for studying the Fourier spectrum during the tidal disruption.

Figure 8(a) plots $h(f)f$ for model A. We also plot the spectra for the analytical third PN waveforms (dotted curve) and for the purely numerical waveforms with no matching (dashed curve). For $\pi M_0 f \ll 1$, the spectra of the matched and PN waveforms behave [7] as

$$h(f)f = \sqrt{\frac{5}{24\pi}}\eta^{1/2}(\pi M_0 f)^{-1/6}. \quad (33)$$

We note that the effective amplitude defined by the average over the source direction and the direction of the binary orbital plane is

$$h_{\rm eff} \equiv \frac{2}{5}\frac{h(f)fM_0}{D} = 9.6\times 10^{-23}\left(\frac{h(f)f}{0.1}\right)\left(\frac{M_0}{5M_\odot}\right)\left(\frac{D}{100\ {\rm Mpc}}\right)^{-1}. \quad (34)$$

Thus, the effective amplitude is $\approx 10^{-22}$ at $f \approx 1$ kHz for $D = 100$ Mpc and $M_0 = 5M_\odot$.

It is found that the spectrum for the purely numerical data agrees with the spectrum of the matched data for $f \gtrsim 800$ Hz besides the spurious modulation for the spectrum of the purely numerical data which results from the incomplete data sets for the inspiral phase. Here, $f = 800$ Hz is slightly smaller than $f_{\rm tidal}$ predicted from Eq. (5) (see also Table IV). This illustrates that the matching does not affect the global shape of the spectrum for $f \gtrsim f_{\rm tidal}$.

We still see the modulation and dip of the spectrum for the matched data in the frequency band between $\sim$500 and 800 Hz. The possible physical reason for the dip at $f \lesssim 1$ kHz is that the radial-approach velocity of the BH and NS steeply increases near the ISCO ($f \sim 1.2$ kHz), and hence the integration time for gravitational waves decreases. As a result, the effective amplitude at such a high-frequency band slightly decreases. This feature is well known for the NS-NS merger [53]. However, there

TABLE IV. The expected frequency of gravitational waves at the tidal disruption $f_{\rm tidal}$, the peak frequency of gravitational wave spectrum near the sharp cutoff in the high-frequency region $f_{\rm cut}$, and the ratio $f_{\rm cut}/f_{\rm tidal}$.

Model	$f_{\rm tidal}$ (kHz)	$f_{\rm cut}$ (kHz)	$f_{\rm cut}/f_{\rm tidal}$
A	0.856	1.16	1.36
B	0.997	1.41	1.41
C	0.736	0.92	1.25
D	0.877	1.14	1.30
E	1.021	1.40	1.37
F	0.840	1.09	1.30

are also possible unphysical reasons, as follows: (i) the orbit of the BH-NS binary has a nonzero eccentricity because the initial data do not provide an exactly circular orbit [28], and (ii) the matching of the numerical and PN data induces a systematic error. Thus, the spectrum for this band may not be very accurate. We do not pay attention to this low-frequency band in the following.

The noteworthy feature of the spectrum is that the spectrum amplitude does not damp even for $f_{\rm tidal} < f \lesssim 1.3 f_{\rm tidal} \equiv f_{\rm cut}$ [see the solid circles in Figs. 8(b)–8(d) for the approximate location of $f_{\rm cut}$]. The reason for this is that the NS orbiting near the ISCO has a radial-approach velocity of order ~10% of the orbital velocity due to the radiation reaction of gravitational waves, and hence the NS is not immediately tidally disrupted at the orbit of $f = f_{\rm tidal}$, although the tidal disruption of the NS likely sets in at $f = f_{\rm tidal}$. As a result, the inspiral orbit is maintained for a while even inside the predicted tidal disruption orbit, and gravitational waves of a large amplitude are emitted for $f > f_{\rm tidal}$. Because the NS is completely disrupted at $f \approx f_{\rm cut} > f_{\rm tidal}$, it is not straightforward to determine $f_{\rm tidal}$ from the spectrum of gravitational waves.

We note that our finding of $f_{\rm cut} > f_{\rm tidal}$ is the unique feature for the BH-NS binaries. If the companion of a BH is not as compact as NSs (e.g., for the BH-white dwarf binaries), $f_{\rm cut}$ would be approximately equal to $f_{\rm tidal}$ because the radial-approach velocity due to the gravitational radiation reaction is negligible and hence the tidal disruption would finish at the predicted tidal disruption orbit.

Because the amplitude of gravitational waves quickly decreases after the NS is completely disrupted, the spectrum also sharply falls for the high-frequency band; i.e., above a cutoff frequency $f_{\rm cut}$, the spectrum amplitude steeply decreases. Figure 8(a) shows that for model A, the value of $f_{\rm cut}$ is approximately 1.16 kHz (i.e., $M_0\Omega \approx 0.094$). This confirms the finding in Sec. IV F that the quick decrease of the gravitational wave amplitude occurs near the ISCO in this case.

To see the dependence of the spectrum shape on the mass ratio and NS radius, we plot Figs. 8(b)–8(d). Figures 8(b) and 8(c) compare the spectra for models A, D, and F ($R_{\rm NS} = 13.2$ km) and for models B and E ($R_{\rm NS} = 12.0$ km), for which the NS radii are identical to each other, whereas the mass ratio q is different. It is found that the spectrum shape depends weakly on the mass ratio. The reason for this is that the gravitational wave frequency at which the tidal disruption occurs is determined primarily by the radius and mass of the NS. For models A, D, and F, $f_{\rm cut} \sim 1.1$–1.2 kHz, and for models B and E, $f_{\rm cut} \sim 1.4$ kHz (see Table IV). Obviously, for the smaller radii, the value of $f_{\rm cut}$ is larger because the NS is completely disrupted for the smaller orbital separation.

We also calculate the ratio of $f_{\rm cut}$ to $f_{\rm tidal}$ (see Table IV). For models A, D, and F, the ratio is ~1.3, whereas for models B and E, it is slightly larger, ~1.4. The reason is that the compact NS has the larger radial-approach velocity at $f = f_{\rm tidal}$, and hence the NS is completely disrupted at a smaller orbital separation.

Figure 8(d) compares the spectra for models A–C, for which the mass ratio q is approximately identical, whereas the NS radii are different. We find that the value of $f_{\rm cut}$ depends strongly of the NS radius and is smaller for larger NS radii, indicating that the tidal disruption sets in at a larger orbital separation. The ratio $f_{\rm cut}/f_{\rm tidal}$ is also smaller for larger NS radii (see Table IV). The reason for this is that, for the larger NS, the tidal disruption sets in at a larger orbital separation, and hence the radial-approach velocity is smaller. However, even for model C, the ratio is ≈ 1.25. This implies that gravitational waves of a high amplitude are emitted well inside the orbit of the onset of tidal disruption, even for a less compact NS of nearly upper-limit radius ~15 km.

Finally, we note the following: Fig. 8 and Eq. (34) show that the effective amplitude at $f = f_{\rm cut} \sim 1$ kHz is $\approx 10^{-22}$ for the typical distance and total mass as $D = 100$ Mpc and $M_0 = 5M_\odot$. Even for the optimistic direction of the source and its binary orbital plane, the effective amplitude is at most $\approx 2.5 \times 10^{-22}$. The designed sensitivity of the advanced LIGO is $\sim 3 \times 10^{-22}$ at $f \sim 1$ kHz [54]. This implies that it will not be possible to detect gravitational waves during the tidal disruption by the detectors of standard design for $D \gtrsim 100$ Mpc. To detect gravitational waves at such high frequency, the detectors of a special instrument (e.g., resonant-side band extraction [55]) which is sensitive to high-frequency gravitational waves is necessary.

V. SUMMARY

We have presented the numerical results of fully general relativistic simulation for the merger of BH-NS binaries, focusing on the case that the NS is tidally disrupted by a nonspinning low-mass BH of $M_{\rm BH} \approx 3.3$–$4.6M_\odot$. The Γ-law EOS with $\Gamma = 2$ and an irrotational velocity field are employed for modeling the NSs. To see the dependence of the tidal disruption event on the NS radius, we choose it in a wide range as $R_{\rm NS} = 12.0$–1.47 km, whereas the NS mass is fixed to $\approx 1.3M_\odot$. The resulting

mass ratio $q \equiv M_{\rm NS}/M_{\rm BH}$ is in the range between ≈ 0.28 and 0.4.

As predicted by the study for the quasicircular states [3,4], for all the chosen models, the NS is tidally disrupted at orbits close to the ISCO. The BH of the spin of 0.5–0.6 is formed and a large fraction of the material is quickly swallowed by the BH, whereas 2%–12% of the material forms a hot and compact torus around the BH. The resultant mass and density of the torus depend strongly on the mass ratio q and NS radius $R_{\rm NS}$, in particular, on $R_{\rm NS}$. For $R_{\rm NS} = 12.0$ km, the torus mass is at most $0.05M_\odot$, even for the large value of the mass ratio $q \approx 0.39$. For $R_{\rm NS} = 14.7$ km, by contrast, the torus mass can be $\gtrsim 0.1M_\odot$ for $q \approx 0.33$. Extrapolating the results in this paper, the torus mass would be smaller than $0.01M_\odot$ for $R_{\rm NS} = 11$ km, even for $q \sim 0.4$. The stiff nuclear EOSs predict the radius of ≈ 11–12 km for $M_{\rm NS} = 1.3M_\odot$–$1.4M_\odot$ [31]. This suggests that the torus mass is likely to be $\ll 0.1M_\odot$, even for the BH mass $3M_\odot$–$4M_\odot$. This point should be more rigorously clarified for the future simulation employing the realistic nuclear EOSs.

For the optimistic case in which $R_{\rm NS} \gtrsim 13$ km or $q \gtrsim 0.4$, the torus mass can be $\gtrsim 0.05M_\odot$. As we found from the value of the $\varepsilon_{\rm th}$, the resultant torus likely has high temperature, 10^{10}–10^{11} K. This suggests that such outcomes are promising candidates for driving SGRBs. According to the latest simulations for the hot and compact torus around the BH by Setiawan *et al.* [44], the total energy deposited by neutrino-antineutrino annihilation is $\sim 10^{49}(M_{\rm torus}/0.01M_\odot)$ ergs for $0.01M_\odot \lesssim M_{\rm torus} \lesssim 0.1M_\odot$ and $a = 0.6$. Here, $M_{\rm torus}$ is the initial torus mass for the simulation. Assuming that the conversion rate to the gamma-ray energy is 10% [56], the total energy of SGRBs is $\sim 10^{48}(M_{\rm torus}/0.01M_\odot)$ ergs according to their numerical results. This indicates that if the NS radius is $\gtrsim 13$ km with $M_{\rm BH} = 3.3M_\odot$–$4M_\odot$, the SGRB of the total energy $\sim 10^{49}$ ergs may be driven. By contrast, for $R_{\rm NS} \lesssim 12$ km with $M_{\rm BH} \gtrsim 3.3M_\odot$, the total energy is likely to be at most several $\times 10^{48}$ ergs; i.e., only the weak SGRBs can be explained. We note that the final spin parameter depends on the initial spin of the BH. In the merger of the rapidly rotating BH and NS, the resulting spin of the BH will be close to unity. For such BHs, the total deposited energy will be enhanced by the spin effects [46].

Gravitational waves are also computed. It is found that the amplitude of gravitational waves damps during the tidal disruption, and when the NS is completely disrupted, the amplitude becomes much smaller than that at the last inspiral orbit. Although we find that the waveforms in the final phase of the tidal disruption are characterized by a QNM, its amplitude is much smaller than that of gravitational waves at the last inspiral phase, in particular, for the large value of $R_{\rm NS}$. The reason for this is that the NS is tidally disrupted before plunging into the BH, and hence a significant excitation of the QNM by the coherently infalling material is not achieved, in contrast to the BH-BH merger (e.g., [18,19,32,33]). For the case that the NS is compact with $R_{\rm NS} = 12$ km, the tidal disruption occurs at an orbit very close to the ISCO and a large amount of the material falls fairly coherently into the BH, resulting in a relatively high amplitude of gravitational waves associated with a QNM. However, the amplitude is still much smaller than that at the last inspiral orbit.

The Fourier spectrum of gravitational waves is also analyzed. Because the amplitude of gravitational waves quickly damps during the tidal disruption, the spectrum amplitude steeply decreases above a cutoff frequency $f_{\rm cut}$. The noteworthy feature is that the cutoff frequency does not agree with the predicted frequency at which the tidal disruption sets in, $f_{\rm tidal}$. The reason for this is that the NS in the compact binaries has a radial-approach velocity of order $\sim 10\%$ of the orbital velocity and is not immediately tidally disrupted at $f = f_{\rm tidal}$. We have found that $f_{\rm cut}/f_{\rm tidal}$ is in the range between 1.25 and 1.4 in our results, depending primarily on the NS radius $R_{\rm NS}$; this value is larger for the smaller values of $R_{\rm NS}$. These results imply that it is not straightforward to determine $f_{\rm tidal}$ from gravitational wave observation. If the dependence of $f_{\rm cut}/f_{\rm tidal}$ on the NS radius and mass ratio is clarified in detail by the numerical simulation, $f_{\rm tidal}$ may be inferred from $f_{\rm cut}$. If such a relation is found, $f_{\rm cut}$ will be useful for determining the properties of NSs, such as the radius and density profile. For this purpose, a detailed simulation taking into account the nuclear EOSs is necessary. We plan to perform such a simulation in the next step.

ACKNOWLEDGMENTS

We deeply thank members in the Meudon Relativity Group, in particular, Eric Gourgoulhon, for developing the free library LORENE, which is used for computation of the initial conditions. Numerical computations were performed on the FACOM-VPP5000 at CfCA at the National Astronomical Observatory of Japan and on the NEC-SX8 at the Yukawa Institute of Theoretical Physics of Kyoto University. This work was supported by Monbukagakusho Grant No. 19540263.

APPENDIX A: COMPARISON WITH THE DIFFERENT GRID-RESOLUTION RESULTS

In this appendix, we present the results for models A0, A1, A2, and C2, for which the physical parameters of the initial conditions are the same as those for models A and C but the simulations were performed with different grid resolutions (see Table II).

Figure 9 plots the evolution of the rest mass of the material located outside the apparent horizon $M_{r>r_{\rm AH}}$ and the area of the apparent horizon in units of $16\pi M^2$ for models A0, A1, A2, and C2. For comparison, the results for models A and C are shown together.

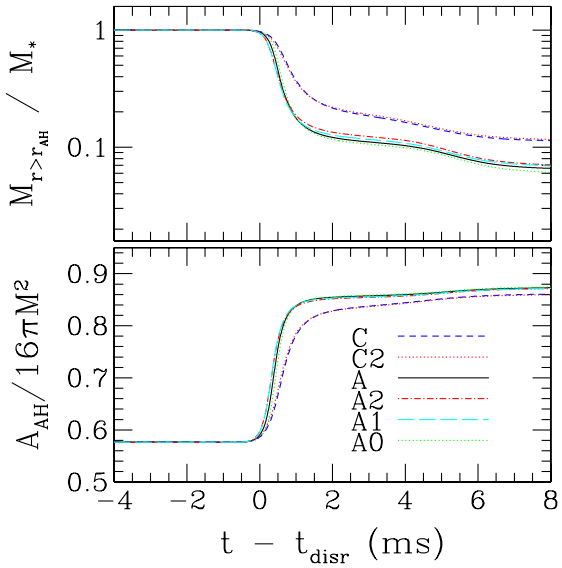

FIG. 9 (color online). The same as Fig. 6(c) but for models A, C, A0, A1, A2, and C2. We choose the values of $t_{\rm disr} = 4.30$ ms, 4.17 ms, 4.75 ms, and 4.25 ms for A2, A1, A0, and C2, respectively. For models A and C, see the caption of Fig. 6.

We find that the results for models A0, A1, and A2 agree qualitatively well with those for model A, although a quantitative difference is seen. Because of the difference of the grid structure for covering the BH and NS and/or because of the larger numerical dissipation for the lower-resolution runs, the time of the onset of tidal disruption $t_{\rm disr}$ slightly disagrees among the four models, but the difference is only ≈ 0.2–0.3 ms ($\sim 10\%$ of the orbital period at the last inspiral orbit). The values of $M_{r>r_{\rm AH}}$ ($A_{\rm AH}/16\pi M^2$) are systematically overestimated (underestimated) for the lower-resolution runs. The reason for the overestimation of $M_{r>r_{\rm AH}}$ is likely to be that, with poorer grid resolutions, angular momentum is spuriously transported to spread the matter outward. Although the values systematically vary, the order of the convergence is not exactly determined because the values fluctuate. The likely reason for this is that the grid structure is different for each simulation. We also note that the order of the convergence in the presence (absence) of shocks should be the first (third) order for the hydro part, whereas that for the gravitational field is fourth order, and thus the order of the convergence is not simply determined.

Because the values of $M_{r>r_{\rm AH}}$ and $A_{\rm AH}$ systematically vary with varying the grid resolution, it is natural to consider that the results approach convergent values. To conservatively estimate the convergent values, we assume that the first-order convergence holds for $M_{r>r_{\rm AH}}$ and $A_{\rm AH}$. Then, the extrapolation by the least-square fitting gives the value of $M_{r>r_{\rm AH}}$ at $t - t_{\rm disr} = 5$ and 7 ms for $\Delta x \to 0$ is ≈ 0.075 and $0.050 M_\odot$, and hence the errors for $M_{r>r_{\rm AH}}$ at $t - t_{\rm disr} = 5$ and 7 ms are $\sim 0.06 M_\odot$ and $\sim 0.05 M_\odot$ for model A2 and $\sim 0.05 M_\odot$ and $\sim 0.04 M_\odot$ for model A, respectively. Therefore, the torus mass may be overestimated by a factor of ~ 2. By contrast, for $A_{\rm AH}/16\pi M^2$, the relative errors at $t - t_{\rm disr} = 5$ and 7 ms are small, $\sim 1.4\%$ and 1.4% for model A2 and $\sim 1.1\%$ and 1.0% for model A, respectively.

We find that the results for model C2 agree with those for model C in a better manner. In this case, the time of the onset of tidal disruption $t_{\rm disr}$ agrees only with a difference ≈ 0.05 ms ($\sim 2\%$ of the orbital period at the last inspiral orbit). Furthermore, the value of $M_{r>r_{\rm AH}}$ and the area of the apparent horizon agree within $\sim 3\%$ and $\sim 0.1\%$ errors, respectively. As in the case of model A, the values of $M_{r>r_{\rm AH}}$ ($A_{\rm AH}$) are overestimated (underestimated) for the lower resolution. Assuming the first-order convergence, the exact values of $M_{r>r_{\rm AH}}$ and $A_{\rm AH}/16\pi M^2$ at $t - t_{\rm disr} = 7$ ms are inferred, and by comparison with these values, we find that the errors of $M_{r>r_{\rm AH}}$ and $A_{\rm AH}/16\pi M^2$ at $t - t_{\rm disr} = 7$ ms for model C (C2) are $\sim 11\%$ (14%) and $\sim 0.5\%$ (0.7%), respectively.

For model C2, the grid spacing for the inner computational domain is $\Delta x = M_{\rm p}/12$, with which the major diameter of the NS is covered by the 50 grid points (see Table II). With such a setting, the orbits of the BH and NS are computed with an accuracy enough at least for the qualitative study. For determining the more convergent results, it is necessary to perform simulations with better accuracy. However, the error behaves systematically, and for the qualitative study, the present simulation setting appears to be acceptable.

Figure 10 plots h_+ and $h_\times$ (a) for models A and A2 and (b) for models C and C2. This shows that the waveforms for the high- and low-resolution runs agree qualitatively well. For the inspiral phase, the difference of the waveforms for the two different resolutions is very small. In particular, for models C and C2, the amplitudes at a given time agree with each other within $\sim 3\%$ error for $t_{\rm ret} \lesssim 4.5$ ms. During the tidal disruption phase, the amplitude is systematically smaller for the low-resolution runs. The possible reason for this is that the compactness of the NS is more quickly lost with the lower resolution, resulting in the less coherent excitation of gravitational waves. However, the difference of the amplitude is still at most $\sim 10\%$ for model C2. For model A2, the error is larger, in particular, for 4.5 ms $\lesssim t_{\rm ret} \lesssim 5$ ms, although the waveforms agree qualitatively with those for model A. The primary source of the error is the phase difference caused by the fact that, for the lower resolution, the tidal disruption sets in earlier. During the tidal disruption, the wave amplitude for model A2 is by a factor of ~ 2 smaller than that for model A. This indicates that the simulation of the poor resolution significantly underestimates the amplitude during the tidal disruption phase. Because of the underestimation of the amplitude, the total energy and angular momentum emitted by gravitational waves are underestimated by $\sim 5\%$ for model C2 and by $\sim 10\%$ for model A2 in comparison with models C and A.

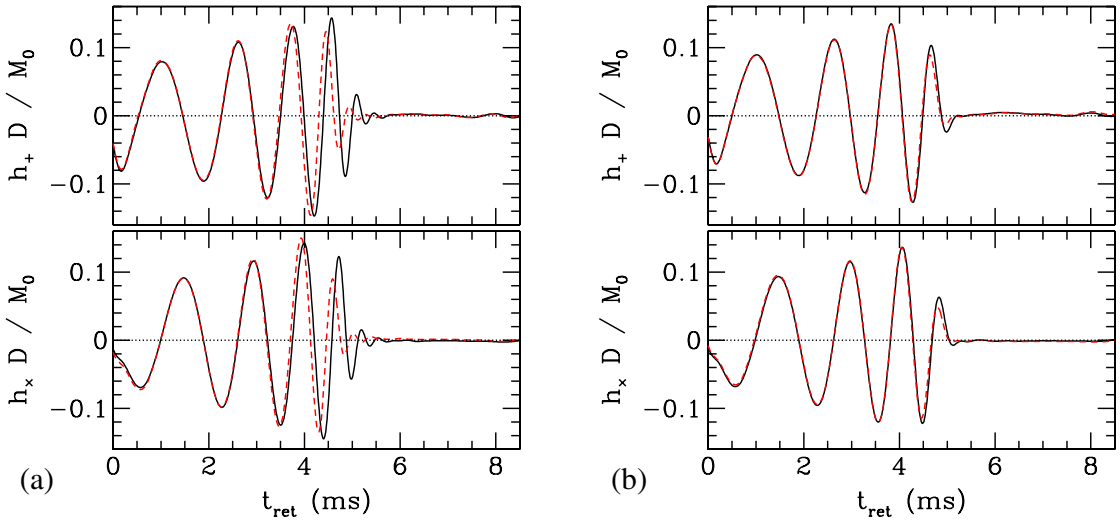

FIG. 10 (color online). The same as Fig. 7(c) but (a) for models A (solid curves) and A2 (dashed curves) and (b) for models C (solid curves) and C2 (dashed curves), respectively.

APPENDIX B: SIMULATION OF SMALLER INITIAL ORBITAL SEPARATIONS

At birth of BH-NS binaries in nature, the orbital separation is much larger than the NS radius, and then it gradually decreases as a result of gravitational radiation to merger. This implies that for a realistic study of BH-NS merger, it is necessary to prepare an initial condition of sufficiently large orbital separation and then to follow many cycles of the inspiral phase. However, it is not feasible to perform such a simulation with our current numerical code and computational resources. We only followed the inspiral phase of the binary by about one-and-half orbits. For studying the influence of such small initial orbital separation on the results, we performed two test simulations of smaller initial orbital separations than for model A, choosing $M_0\Omega_0 = 0.045$ and 0.050 (models Ab and Ac, respectively; see Table I). Note that $M_0\Omega_0 \approx 0.040$ for model A. For all the cases, the grid spacing in the inner uniform zone is the same as that for model A ($\Delta x = M_p/15$). The outer boundary is located at $L \approx 0.86\lambda_0$ appropriately varying N and N_0, whereas ξ and Δi are fixed to be 20.5 and 30, respectively. For models Ab and Ac, the tidal disruption sets in at about one-and-quarter orbits and about one orbit, respectively.

Figure 11 plots the evolution of the rest mass of the material located outside the apparent horizon $M_{r>r_{\rm AH}}$ and the area of the apparent horizon in units of $16\pi M^2$ for models A, Ab, and Ac. We find that for larger initial orbital angular velocity, $M_{r>r_{\rm AH}}$ after the merger is systematically smaller (and as a result, the area of the BH is larger). The reason for this is that with too large initial orbital angular velocity, the inspiral time is too short to transport the angular momentum inside the NS by the tidal torque during the inspiral phase. For models A, Ab, and Ac, the value of $M_{r>r_{\rm AH}}$ at $t - t_{\rm disr} = 7$ ms is $\approx 0.096M_\odot$, $0.065M_\odot$, and $0.031M_\odot$. Because the magnitude of the tidal torque is proportional to the square of the angular velocity, Ω^2, and inspiral time is approximately proportional to $\Omega^{8/3}$, one can expect that this value will relax to a convergent value for the initial condition of smaller $M_0\Omega_0$. For example, if we choose $M_0\Omega_0 = 0.03$ as an initial condition, the inspiral time would be about twice as long as that for $M_0\Omega_0 = 0.04$, and hence the value of $M_{r>r_{\rm AH}}$ might relax approximately to a convergent value. Extrapolating the present results for $M_0\Omega_0 \to 0.03$, we find that the torus mass may be by a factor of $\sim$1.6 larger than that for $M_0\Omega_0 = 0.04$, and for the initial condition with $M_0\Omega_0 =$

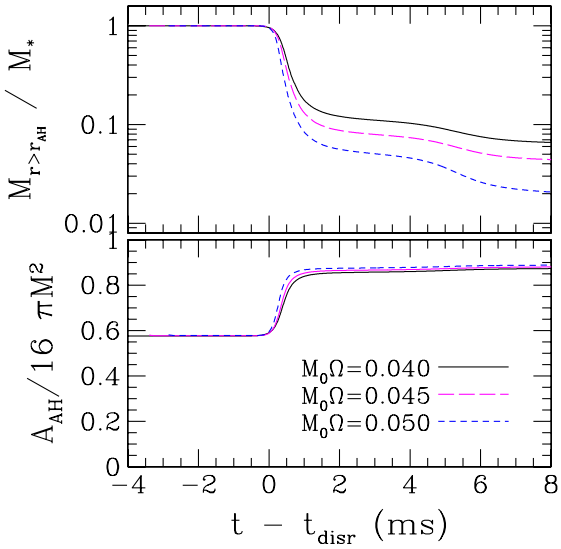

FIG. 11 (color online). The same as Fig. 9 but for models A (solid curves), Ab (long-dashed curves), and Ac (dashed curves). For models Ab and Ac, $t_{\rm disr}$ is chosen to be 3.4 and 2.85 ms, respectively.

0.04, the torus mass might be underestimated by a factor of $\sim 60\%$.

Because $M_0\Omega_0 = 0.04$ for all the models in the present simulations, the torus mass is systematically underestimated. To determine the final torus mass within $0.01M_\odot$ error, the initial orbital angular velocity should be $M_0\Omega_0 \lesssim 0.03$, and such a simulation is left for future work. However, the systematic underestimation even by a factor of ~ 2 does not change the conclusion about the formation process of the torus, the order of the torus mass, and its dependence on the NS radius. By contrast, if we choose an initial condition with $M_0\Omega_0 > 0.05$, we would reach a wrong conclusion such as that the torus is not formed after the merger.

Figure 12 compares h_+ and $h_\times$ for models A and Ab. For model Ab, we plot $-h_+$ and $-h_\times$ as a function of $t_{\rm ret} + 1$ ms (the time is shifted for comparison of the wave phase). This figure indicates that the waveforms agree qualitatively well; both waveforms are composed of the inspiral, merger, and ring-down phases. Furthermore, the wave phase agrees fairly well, although a slight difference associated with the difference in the initial condition is seen. This illustrates that for the qualitative study of the gravitational waveforms in the merger phase, the large initial orbital angular velocity adopted in this paper does not cause serious problems.

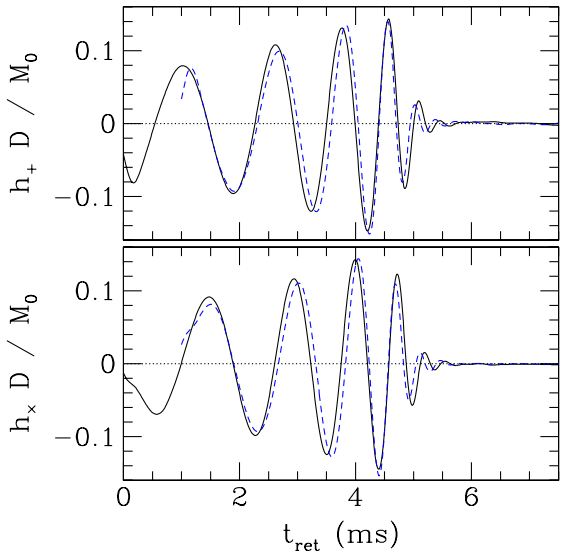

FIG. 12 (color online). The same as Fig. 10 but for models A (solid curves) and Ab (dashed curves). For model Ab, we plot $-h_+$ and $-h_\times$ as a function of $t_{\rm ret} + 1$ ms.

[1] I. H. Stairs, Science **304**, 547 (2004).
[2] R. Voss and T. M. Taulis, Mon. Not. R. Astron. Soc. **342**, 1169 (2003); K. Belczynski, T. Bulik, and B. Rudak, Astrophys. J. **571**, 394 (2002); V. Kalogera *et al.*, Astrophys. J. **601**, L179 (2004); Phys. Rep. **442**, 75 (2007).
[3] K. Taniguchi, T. W. Baumgarte, J. A. Faber, and S. L. Shapiro, Phys. Rev. D **75**, 084005 (2007).
[4] K. Taniguchi, T. W. Baumgarte, J. A. Faber, and S. L. Shapiro, Phys. Rev. D **77**, 044003 (2008).
[5] M. Ishii, M. Shibata, and Y. Mino, Phys. Rev. D **71**, 044017 (2005).
[6] L. Blanchet, Living Rev. Relativity **9**, 4 (2006).
[7] For example, C. Cutler and E. E. Flanagan, Phys. Rev. D **49**, 2658 (1994).
[8] L. Lindblom, Astrophys. J. **398**, 569 (1992).
[9] M. Vallisneri, Phys. Rev. Lett. **84**, 3519 (2000).
[10] C. L. Fryer, S. E. Woosley, M. Herant, and M. B. Davies, Astrophys. J. **520**, 650 (1999).
[11] E. Barger, AIP Conf. Proc. **836**, 33 (2006).
[12] W. H. Lee and W. Kluzniak, Astrophys. J. **526**, 178 (1999); H. T. Janka, T. Eberl, M. Ruffert, and C. L. Fryer, Astrophys. J. **527**, L39 (1999).
[13] J. A. Faber, T. W. Baumgarte, S. L. Shapiro, and K. Taniguchi, Astrophys. J. **641**, L93 (2006).
[14] J. A. Faber, T. W. Baumgarte, S. L. Shapiro, K. Taniguchi, and F. A. Rasio, Phys. Rev. D **73**, 024012 (2006).
[15] M. Shibata and K. Uryū, Phys. Rev. D **74**, 121503(R) (2006); Classical Quantum Gravity **24**, S125 (2007).
[16] M. Shibata, K. Taniguchi, and K. Uryū, Phys. Rev. D **68**, 084020 (2003).
[17] M. Shibata, K. Taniguchi, and K. Uryū, Phys. Rev. D **71**, 084021 (2005); M. Shibata and K. Taniguchi, *ibid.* **73**, 064027 (2006).
[18] M. Campanelli, C. O. Lousto, P. Marronetti, and Y. Zlochower, Phys. Rev. Lett. **96**, 111101 (2006); J. G. Baker, J. Centrella, D.-I. Choi, M. Koppitz, and J. van Meter, Phys. Rev. Lett. **96**, 111102 (2006).
[19] B. Brügmann, J. A. Conzalez, M. Hannam, S. Husa, and U. Sperhake, arXiv:gr-qc/0610128.
[20] C. S. Kochanek, Astrophys. J. **398**, 234 (1992); L. Bildsten and C. Cutler, *ibid.* **400**, 175 (1992).
[21] M. Shibata, Phys. Rev. D **58**, 024012 (1998); S. A. Teukolsky, Astrophys. J. **504**, 442 (1998).
[22] E. Gourgoulhon, P. Grandclément, K. Taniguchi, J.-A. Marck, and S. Bonazzola, Phys. Rev. D **63**, 064029 (2001).
[23] K. Taniguchi and E. Gourgoulhon, Phys. Rev. D **66**, 104019 (2002); **68**, 124025 (2003).
[24] LORENE website: http://www.lorene.obspm.fr/.
[25] P. Grandclément, Phys. Rev. D **74**, 124002 (2006); **75**, 129903(E) (2007).
[26] K. Taniguchi, T. W. Baumgarte, J. A. Faber, and S. L. Shapiro, Phys. Rev. D **72**, 044008 (2005).
[27] Z. B. Etienne, J. A. Faber, Y. T. Liu, S. L. Shapiro, K. Taniguchi, and T. W. Baumgarte, Phys. Rev. D (to be published).
[28] E. Berti, S. Iyer, and C. M. Will, arXiv:gr-qc/0709.2589.

[29] Because of the rescale invariance, the present numerical results may be interpreted as those for different physical values. For example, the results for model A may be regarded as those for the merger between a NS of $M_* = 1.300M_\odot$, $M_{\rm NS} = 1.209M_\odot$, and $R_{\rm NS} = 12.3$ km and a BH of $M_{\rm BH} = 3.691M_\odot$.
[30] J. M. Lattimer and M. Prakash, Science **304**, 536 (2004).
[31] For example, A. Akmal, V. R. Pandharipande, and D. G. Ravenhall, Phys. Rev. C **58**, 1804 (1998); F. Douchin and P. Haensel, Astron. Astrophys. **380**, 151 (2001).
[32] A. Buonanno, G. B. Cook, and F. Pretorius, Phys. Rev. D **75**, 124018 (2007).
[33] J. G. Baker, *et al.*, Phys. Rev. D **75**, 124024 (2007); M. Hannam, H. Husa, U. Sperhake, B. Brügmann, and J. A. Gonzalez, Phys. Rev. D **77**, 044020 (2008).
[34] M. Boyle *et al.*, Phys. Rev. D **76**, 124038 (2007).
[35] M. Shibata, Phys. Rev. D **67**, 024033 (2003).
[36] M. Shibata and J. A. Font, Phys. Rev. D **72**, 047501 (2005).
[37] M. Shibata and T. Nakamura, Phys. Rev. D **52**, 5428 (1995).
[38] M. Shibata, Phys. Rev. D **55**, 2002 (1997); M. Shibata and K. Uryū, Phys. Rev. D **62**, 087501 (2000).
[39] V. Moncrief, Ann. Phys. (N.Y.) **88**, 323 (1974).
[40] M. Shibata and Y. I. Sekiguchi, Phys. Rev. D **71**, 024014 (2005).
[41] J. A. Gonzalez, U. Sperhake, B. Brügmann, M. Hannam, and S. Husa, Phys. Rev. Lett. **98**, 091101 (2007).
[42] J. G. Baker *et al.*, Astrophys. J. Lett. **653**, L93 (2006).
[43] R. Popham, S. E. Woosley, and C. Fryer, Astrophys. J. **518**, 356 (1999); R. Narayan, T. Piran, and P. Kumar, Astrophys. J. **557**, 949 (2001); T. DiMatteo, R. Perna, and R. Narayan, Astrophys. J. **579**, 706 (2002); K. Kohri and S. Mineshige, Astrophys. J. **577**, 311 (2002); A. Janiuk, R. Perna, T. DiMatteo, and B. Czerny, Mon. Not. R. Astron. Soc. **355**, 950 (2004); W.-X. Chen and A. M. Beloborodov, Astrophys. J. **657**, 383 (2007).
[44] S. Setiawan, M. Ruffert, and H.-Th. Janka, Mon. Not. R. Astron. Soc. **352**, 753 (2004); Astron. Astrophys. **458**, 553 (2006).
[45] W. H. Lee, E. Ramirez-Ruiz, and D. Page, Astrophys. J. **632**, 421 (2005).
[46] M. Shibata, Y. I. Sekiguchi, and R. Takahashi, Prog. Theor. Phys. **118**, 257 (2007).
[47] In this formula, we ignore the binding energy between the BH and the surrounding material. Thus, $M_{\rm BH,f}$ likely overestimates the true BH mass slightly.
[48] M. Shibata, Phys. Rev. D **76**, 064035 (2007).
[49] E. W. Leaver, Proc. R. Soc. A **402**, 285 (1985); F. Echeverria, Phys. Rev. D **40**, 3194 (1989).
[50] The study of the kick velocity in numerical relativity [41,42,51] has clarified that the numerical results of its magnitude depend sensitively on the initial condition. For the initial condition of small orbital separation, the given quasicircular orbit includes nonrealistic radial velocity and/or nonzero ellipticity. Because of such unrealistic elements, the estimated linear momentum flux includes a systematic error. The results of [41,42,51] show that the systematic error could be as large as the magnitude of the kick velocity. Because the simulation starts from a fairly close orbit in this work, the systematic error may be as large as the magnitude for the kick velocity.
[51] L. Rezzolla *et al.*, arXiv:gr-qc/0708.3999, and references cited therein.
[52] L. Blanchet, M. S. S. Qusailar, and C. M. Will, Astrophys. J. **635**, 508 (2005).
[53] For example, X. Zhuge, J. M. Centrella, and S. L. W. McMillan, Phys. Rev. D **50**, 6247 (1994).
[54] K. S. Thorne, in *Compact Stars in Binaries: The Proceeding of IAU Symposium No. 165* (Kluwer Academic Publishers, Dordrecht, 1996), p. 153.
[55] S. Kawamura (private communication).
[56] For example, M. A. Aloy, H.-T. Janka, and E. Müller, Astron. Astrophys. **436**, 273 (2005).